UNIVERSIDAD DE CONCEPCIÓN

Centro de Investigación en Ingeniería Matemática (CI^{2}MA)

A two-dimensional multilayer shallow water model of tsunami-forest interaction

Raimund Bürger, Cipriano Escalante,
Enrique D. Fernández Nieto, Jorge Moya

PREPRINT 2026-14

SERIE DE PRE-PUBLICACIONES

A TWO-DIMENSIONAL MULTILAYER SHALLOW WATER MODEL OF TSUNAMI-FOREST INTERACTION

RAIMUND BÜRGER[A], CIPRIANO ESCALANTE[B], ENRIQUE D. FERNÁNDEZ-NIETO[C], AND JORGE MOYA[A,C,*]

Abstract. Investigating the interaction of tsunamis with coastal forests is essential for assessing the protective role of coastal vegetation. This interaction can be described by a multilayer shallow-water model in two horizontal space dimensions, which is derived from a free-surface formulation of the Euler equations for an ideal fluid. The resulting governing equations are approximated by a layer-averaged non-hydrostatic (LDNH) approach. Within the LDNH framework pressures are treated as linear functions within each layer and velocities are represented as piecewise constant. Following [K. Iimura, N. Tanaka, Numerical simulation estimating effects of tree density distribution in coastal forest on tsunami mitigation, Ocean Engrg. 54 (20212) 223–232], additional source terms describing drag, inertia, and porosity effects are incorporated to represent momentum exchange between the flow and the forested terrain. These factors are specified in each vertical layer to achieve a more detailed description of vegetation structure than is possible with single-layer formulations. The resulting horizontally two-dimensional multilayer system is approximated numerically by combining projection techniques for the non-hydrostatic pressure with polynomial viscosity finite volume schemes of the PVM class [M. J. Castro, E. D. Fernández-Nieto, A class of computationally fast first order finite volume solvers: PVM methods, SIAM J. Sci. Comput. 34 (2012) A2173–A2196]. This methodology allows efficient simulation of tsunami propagation and onshore inundation in the presence of vegetated landscapes. The model performance and numerical method are assessed through comparisons with laboratory measurements and available observational data. In general good agreement is obtained. The simulations further support the conclusion that coastal vegetation can provide substantial attenuation of tsunami impact and thus serves as a valuable component of natural coastal defense strategies.

Keywords: Finite volume method, layer averaged non-hydrostatic approach, multilayer model, coastal forest, tsunami mitigation.

1. Introduction

1.1. **Scope.** The propagation of tsunamis over coastal regions covered by vegetation is a complex phenomenon involving strong interactions between the incoming wave, the fluid motion within the vegetated layer, and the underlying bathymetry. The accurate representation of these processes is crucial for understanding natural coastal protection mechanisms and for improving predictive models used in risk assessment and mitigation strategies.

Depth-averaged models based on the classical Saint–Venant equations are widely employed for tsunami simulations due to their simplicity and computational efficiency. However, their inherent

Date: April 21, 2026.

*Corresponding author.

[A]CI^{2}MA and Departamento de Ingeniería Matemática, Facultad de Ciencias Físicas y Matemáticas, Universidad de Concepción, Casilla 160-C, Concepción, Chile. E-Mail: rburger@ing-mat.udec.cl, jorgemoya@udec.cl.

[B]Departamento de Matemática Aplicada I, ETS Arquitectura, Universidad de Sevilla, Avda. Reina Mercedes No. 2, 41012 Sevilla, Spain. E-Mail: jmoya1@us.es, edofer@us.es.

[C]Departamento de Matemática Aplicada, Universidad de Málaga, 29071 Málaga, Spain. E-Mail: escalante@uma.es.

assumption of a hydrostatic situation limits their ability to capture vertical accelerations, dispersive effects, and interactions with complex obstacles such as vegetation. To overcome these limitations, various non-hydrostatic and multilayer extensions of the shallow-water equations have been proposed (see, for example, [1, 9]). These formulations account for vertical structure and deviations of pressure from the hydrostatic profile, and thereby provide a more accurate description of free-surface dynamics. The final governing model for a number N of layers can be written as a first-order system of balance equations with non-conservative and source terms as follows. We denote the conservative variables by

$$\boldsymbol{W}_\alpha = \boldsymbol{W}_\alpha(x,y,t) = (h_\alpha, h_\alpha \boldsymbol{u}_\alpha^{\mathrm{T}}, h_\alpha w_\alpha)^{\mathrm{T}}, \quad \alpha = 1,\dots,N, \tag{1.1}$$

where $h_\alpha = h_\alpha(x,y,t)$ the height of layer α that depends on the horizontal coordinates x and y and on time t, $\boldsymbol{u}_\alpha = (u_\alpha, v_\alpha)^{\mathrm{T}} = (u_\alpha, v_\alpha)^{\mathrm{T}}(x,y,t)$ is the horizontal velocity, and $w_\alpha = w_\alpha(x,y,t)$ is the vertical velocity associated with layer α. The sought unknowns are the functions (1.1), which are collected in the vector $\boldsymbol{W} = (\boldsymbol{W}_1,\dots,\boldsymbol{W}_N)^{\mathrm{T}} = \boldsymbol{W}(x,y,t)$. The governing multilayer system of $4N$ scalar partial differential equations (PDEs) can then be written in compact form as

$$\partial_t \boldsymbol{W} + \nabla\cdot \boldsymbol{F}(\boldsymbol{W}) = -\boldsymbol{B}(\boldsymbol{W})\nabla \boldsymbol{W} + \boldsymbol{S}(\boldsymbol{W}), \tag{1.2}$$

where $\nabla = (\partial_x, \partial_y)$ and $\boldsymbol{F}(\boldsymbol{W})$ collects the advective fluxes, $\boldsymbol{B}(\boldsymbol{W})$ contains the non-conservative hydrostatic and interfacial transfer terms, and $\boldsymbol{S}(\boldsymbol{W})$ includes bed slope and frictional forces; these terms will be specified in later parts of the paper. As is common in geophysical applications, (1.2) involves non-conservative terms and source terms.

In [12], a horizontally one-dimensional multilayer non-hydrostatic model was developed to study the attenuation of tsunami waves by coastal forests. That work introduced a finite volume–projection method capable of handling non-hydrostatic pressures, wet-dry interfaces, and vegetation-induced drag, inertia, and porosity effects in a consistent manner. Despite its robustness and physical accuracy, the model was limited to one spatial dimension. Lateral variations and directional effects in the flow field were neglected. It is the purpose of the present work to extend the approach of [12] to a horizontally two-dimensional multilayer non-hydrostatic shallow-water model for tsunami–forest interaction. The new formulation describes the depth-averaged motion of each layer over the (x,y)-plane, incorporating non-hydrostatic pressure corrections, anisotropic vegetation effects, and complex bathymetry. This extension enables the simulation of realistic tsunami propagation patterns, including wave diffraction, channeling between vegetated patches, and spatially varying attenuation across the coastal zone. The model, which can be written in the form (1.2), is discretized using a finite volume (FV) method coupled with a projection step for the non-hydrostatic pressure. The scheme maintains well-balancedness, ensures positivity of the water depth, and accurately treats dry–wet interfaces. Vegetation effects are modelled through drag and porosity tensors that vary spatially, allowing the representation of heterogeneous forest distributions. Numerical experiments demonstrate the capability of the model to reproduce laboratory and field-scale observations, highlighting its potential as a predictive tool for coastal protection analysis.

1.2. **Related work.** Finite volume (FV) schemes are widely used for hyperbolic systems describing geophysical flows. One of the main difficulties associated with FV schemes in these applications is the appropriate treatment of nonconservative products [31], which arise, for instance, in shallow water equations with variable bottom topography [42]. Path-conservative schemes [20, 32, 33] were specifically designed to handle non-conservative products. A particularly useful family of path-conservative schemes are polynomial viscosity matrix (PVM) methods [15] that include several classical schemes such as the Harten-Lax-van Leer (HLL) [26] and Rusanov schemes (also known

as local Lax-Friedrichs (LLF) schemes) as special cases, and which we employ here to deal with the hyperbolic part of the model. See also [17, 29] for general background.

Multilayer shallow water models are a natural choice for the computation of flows in domains whose horizontal extension is much larger than the vertical, and where one wishes to avoid solving the full three-dimensional Navier-Stokes equations while keeping some vertical information. These models were originally developed by Audusse, Bristeau, Sainte-Marie, and coworkers [2, 6, 7, 8, 10]. They were later extended to stratified and viscous flows [24, 25] and also to sedimentation problems [13, 14, 23]. The model studied in the present work fits into this family but adds a non-hydrostatic pressure unknown in each layer. In fact, standard shallow water models assume hydrostatic pressure, which means they miss vertical acceleration, and therefore, dispersive effects. One way to recover these effects consists in formulating a Boussinesq-type model by introducing high-order derivatives for the unknowns. A cleaner way to recover these effects is to include a non-hydrostatic pressure correction directly. A hierarchy of such models, starting from the Euler equations and averaging layer by layer, was derived in [25, 34, 36, 37]. Our model is the lowest-order member of this hierarchy, the so-called LDNH0 model. Numerical aspects like well-balancing and wet-dry treatment for these models were addressed in [4, 16, 28].

The non-hydrostatic pressure correction requires solving an elliptic problem for the pressure in each layer and time iteration. This is achieved by following the projection approach by Chorin and Temam [18, 19, 41]. This idea was adapted to non-hydrostatic shallow water flows by Escalante et al. [21]. The present work essentially extends the approach of [21] to the horizontally two-dimensional multilayer setting, where an additional complication arises from the inertia effects (described below). Regarding the application side, we comment that coastal forests are known to reduce tsunami impact significantly [27, 35, 38, 39, 40, 43]. Modelling the interaction between the flow and the forest introduces drag, porosity, and inertia forces. A horizontally one-dimensional multilayer model including these effects was introduced in [12]. The present work extends that model to two dimensions, which is the main new contribution from the modelling point of view.

1.3. **Outline of the paper.** This article is organized as follows. Section 2 introduces the governing equations of the two-dimensional multilayer non-hydrostatic system. Section 3 describes the numerical method, including the FV discretization and the pressure projection step. Section 4 presents numerical experiments assessing the performance of the proposed scheme. Finally, Section 5 summarizes the main findings and outlines directions for future research.

2. Formulation of the model

2.1. **Layer-wise balance equations.** We consider an incompressible, homogeneous fluid with a free surface elevation $\eta = \eta(x, y, t)$ over a bottom given topography $z_\mathrm{b} = z_\mathrm{b}(x, y)$ (see Figure 1). The total water depth $h = h(x, y, t)$ is defined as $h \coloneqq \eta - z_\mathrm{b}$. The flow domain is vertically discretized into N layers of variable thickness $h_\alpha = h_\alpha(x, y, t)$ such that $h(x, y, t) = h_1(x, y, t) + \cdots + h_N(x, y, t)$ for all x, y and t. We denote by $z_{\alpha+1/2}$ the interface between layers α and $\alpha + 1$. The vertical position of this interface is then given by $z_{\alpha+1/2} = z_\mathrm{b} + h_1 + \cdots + h_\alpha$. Each layer is associated with a depth-averaged horizontal velocity $\boldsymbol{u}_\alpha = (u_\alpha, v_\alpha)^\mathrm{T}$, a representative vertical velocity w_α, and a non-hydrostatic pressure correction q_α that accounts for deviations from hydrostatic equilibrium.

The balance equations for layer α arise from the mass and linear momentum balance formulated for each layer [5, 9] and can be written as

$$\partial_t h_\alpha + \nabla \cdot (h_\alpha \boldsymbol{u}_\alpha) = \Gamma_{\alpha+1/2} - \Gamma_{\alpha-1/2}, \tag{2.1}$$

$$\partial_t (h_\alpha \boldsymbol{u}_\alpha) + \nabla \cdot (h_\alpha \boldsymbol{u}_\alpha \otimes \boldsymbol{u}_\alpha) + g h_\alpha \nabla h = -g h_\alpha \nabla z_\mathrm{b} - \boldsymbol{\tau} - \boldsymbol{F}_\alpha^\mathrm{nh} - \boldsymbol{S}_\alpha^\mathrm{veg}, \tag{2.2}$$

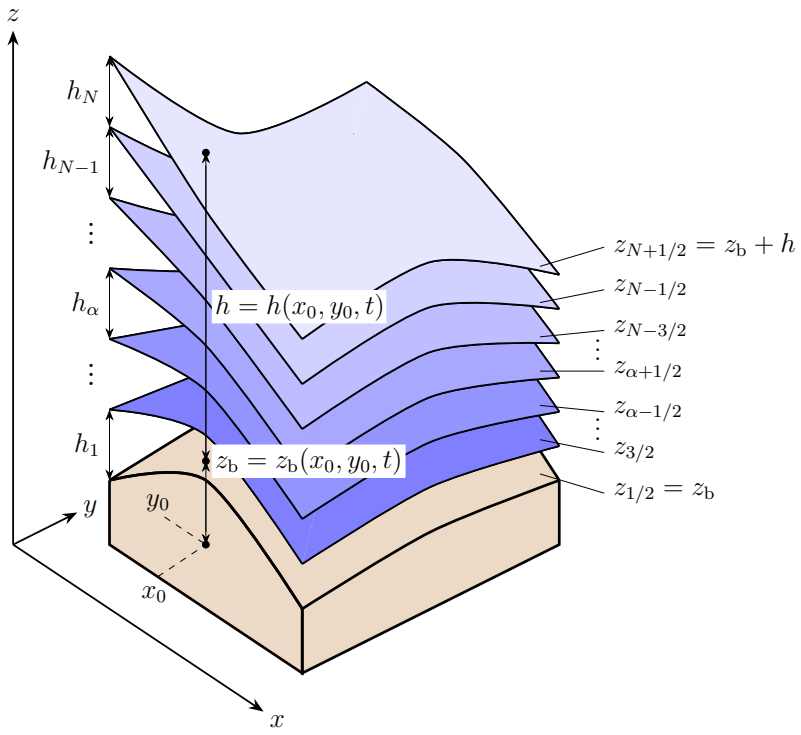

FIGURE 1. Schematic representation of the vertical multilayer discretization above the (x, y)-plane.

where the terms $\Gamma_{\alpha\pm1/2}$ represent mass exchanges between adjacent layers due to vertical velocity. Moreover, $\boldsymbol{\tau}$ denotes the drag force induced by bottom friction, $\boldsymbol{F}_\alpha^{\mathrm{nh}}$ represents the non-hydrostatic pressure correction, and $\boldsymbol{S}_\alpha^{\mathrm{veg}}$ collects the vegetation-induced forces, including drag, inertia, and porosity effects. The combination of these contributions describes the horizontal dynamics of each layer within the multilayer structure.

The non-hydrostatic correction $\boldsymbol{F}_\alpha^{\mathrm{nh}}$ is given by

$$\boldsymbol{F}_\alpha^{\mathrm{nh}} = \nabla z_{\alpha+1/2} q_{\alpha+1/2} - \nabla z_{\alpha-1/2}\, q_{\alpha-1/2} - \nabla(h_\alpha q_\alpha), \quad \alpha = 1, \ldots, N,$$

where q_α is the non-hydrostatic pressure in the middle of the layer.

The vegetation source term $\boldsymbol{S}_\alpha^{\mathrm{veg}}$ accounts for the resistance exerted by stems, trunks, or roots distributed over the computational domain. It can be expressed as

$$\boldsymbol{S}_\alpha^{\mathrm{veg}} = \boldsymbol{f}_{\mathrm{D},\alpha} + \boldsymbol{f}_{\mathrm{M},\alpha}, \quad \alpha = 1, \ldots, N \tag{2.3}$$

with the contributions

$$\boldsymbol{f}_{\mathrm{D},\alpha} \coloneqq C_{\mathrm{D}} \rho \theta_\alpha |\boldsymbol{u}_\alpha| \boldsymbol{u}_\alpha \quad \text{and} \quad \boldsymbol{f}_{\mathrm{M},\alpha} \coloneqq C_{\mathrm{I}} \rho \theta_\alpha \partial_t \boldsymbol{u}_\alpha,$$

where C_{D} and C_{I} are the drag and inertia coefficients, ρ is the fluid density, and θ_α is a porosity.

At the free surface ($\alpha = N$) and at the bottom ($\alpha = 1$), the boundary conditions

$$\Gamma_{N+1/2} = \Gamma_{1/2} = 0,$$

are imposed to ensure mass conservation across the boundaries; the terms $\Gamma_{\alpha+1/2}$ for $\alpha = 1, \ldots, N-1$ are specified in Section 2.2.

Summing (2.1) over all layers yields the total depth-integrated continuity equation

$$\partial_t h + \nabla \cdot (h\boldsymbol{u}) = 0,$$

where $\boldsymbol{u}$ is defined as

$$\boldsymbol{u} \coloneqq \sum_{\beta=1}^{\alpha} \frac{h_\alpha}{h} \boldsymbol{u}_\alpha.$$

This relation, together with (2.2), forms the basis of the proposed multilayer non-hydrostatic model for two-dimensional free-surface flows.

2.2. **Two-dimensional multilayer** LDNH$_0$ **model.** The extension of the one-dimensional multilayer model [12] to two horizontal dimensions $\boldsymbol{x} = (x, y)$ yields the following balance equations for each layer α:

$$\partial_t h + \frac{1}{\bar{\theta}} \nabla \cdot (h\boldsymbol{u}) = 0, \tag{2.4a}$$

$$\begin{aligned}\partial_t (h_\alpha \boldsymbol{u}_\alpha) + \frac{1}{\theta_\alpha} \nabla \cdot (h_\alpha \boldsymbol{u}_\alpha \otimes \boldsymbol{u}_\alpha) + \theta_\alpha \nabla (h_\alpha q_\alpha) - \theta_\alpha q_{\alpha+1/2} \nabla z_{\alpha+1/2} + \theta_\alpha q_{\alpha-1/2} \nabla z_{\alpha-1/2} \\ = -g h_\alpha \theta_\alpha \nabla \eta + \frac{\Gamma_{\alpha+1/2}}{\theta_\alpha} \tilde{\boldsymbol{u}}_{\alpha+1/2} - \frac{\Gamma_{\alpha-1/2}}{\theta_\alpha} \tilde{\boldsymbol{u}}_{\alpha-1/2} - \boldsymbol{f}_{\mathrm{D},\alpha} - \boldsymbol{f}_{\mathrm{M},\alpha} + \frac{1}{\theta_\alpha} \boldsymbol{K}_{\alpha-1/2} - \frac{1}{\theta_\alpha} \boldsymbol{K}_{\alpha+1/2},\end{aligned} \tag{2.4b}$$

$$\partial_t (h_\alpha w_\alpha) + \frac{1}{\theta_\alpha} \nabla \cdot (h_\alpha w_\alpha \boldsymbol{u}_\alpha) + q_{\alpha+1/2} - q_{\alpha-1/2} = \frac{\Gamma_{\alpha+1/2}}{\theta_\alpha} \tilde{w}_{\alpha+1/2} - \frac{\Gamma_{\alpha-1/2}}{\theta_\alpha} \tilde{w}_{\alpha-1/2}, \tag{2.4c}$$

together with the (layer-wise) incompressibility constraint

$$w_\alpha - w_{\alpha-1} - (\boldsymbol{u}_\alpha - \boldsymbol{u}_{\alpha-1}) \cdot \nabla z_{\alpha-1/2} - \tfrac{1}{2}\big(h_{\alpha-1} \nabla \cdot \boldsymbol{u}_{\alpha-1} + h_\alpha \nabla \cdot \boldsymbol{u}_\alpha\big) = 0, \quad \alpha = 2, \dots, N, \tag{2.5}$$

$$w_1 - \boldsymbol{u}_1 \cdot \nabla z_{\mathrm{b}} - \tfrac{1}{2} h_1 \nabla \cdot \boldsymbol{u}_1 = 0, \tag{2.6}$$

The term $\Gamma_{\alpha+1/2}(\boldsymbol{x}, t)$ represents the mass exchange from layer α to layer $\alpha+1$, taken as positive in the upward direction. It is defined as

$$\Gamma_{\alpha+1/2} = \sum_{\beta=1}^{N} \gamma_{\alpha,\beta} \nabla \cdot (h_\beta \boldsymbol{u}_\beta), \quad \text{where} \quad \gamma_{\alpha,\beta} \coloneqq \begin{cases} 1 - \displaystyle\sum_{k=1}^{\alpha} \frac{\theta_k}{N\bar{\theta}} & \text{for } \alpha \geq \beta, \\ -\displaystyle\sum_{k=1}^{\alpha} \frac{\theta_k}{N\bar{\theta}} & \text{for } \alpha < \beta. \end{cases}$$

Moreover, $\tilde{\boldsymbol{u}}_{\alpha\pm1/2}$ and $\tilde{w}_{\alpha\pm1/2}$ denote interface average velocities that are given by

$$\tilde{\boldsymbol{u}}_{\alpha+1/2} \coloneqq \frac{1}{2}(\boldsymbol{u}_\alpha + \boldsymbol{u}_{\alpha+1}), \qquad \tilde{w}_{\alpha+1/2} \coloneqq \frac{w_\alpha + w_{\alpha+1}}{2}.$$

Finally, the quantities $\boldsymbol{K}_{\alpha\pm1/2}$ denote the viscous or momentum transfer terms between adjacent layers. These terms are vector quantities in two dimensions and generalize the scalar interlayer transfer terms $K_{\alpha\pm1/2}$ used in the one-dimensional formulation.

2.3. **Friction force and shear stress.** The bottom friction force $\boldsymbol{\tau}_\alpha$ acts on the lowest layer ($\alpha = 1$) only. It represents the shear stress between the fluid and the ground. It is defined as

$$\boldsymbol{\tau}_\alpha \coloneqq k_{1,\alpha} \|h_\alpha \boldsymbol{u}_\alpha\| h_\alpha \boldsymbol{u}_\alpha = \begin{cases} \dfrac{g n^2 \|\boldsymbol{u}_1\|}{\theta_1 h_1^{1/3}} \boldsymbol{u}_1 & \text{for } \alpha = 1, \\ \boldsymbol{0} & \text{for } \alpha = 2, \dots, N, \end{cases} \tag{2.7}$$

where n is the Manning coefficient and θ_α denotes the layer porosity.

The upper layers are not directly affected by this bottom friction. However, the shear stress generated at the ground is transmitted upward through the internal viscosity of the fluid. This transmission is modeled by interlayer viscous coupling terms that are defined as

$$\boldsymbol{K}_{\alpha+1/2} \coloneqq \begin{cases} \boldsymbol{0} & \text{for } \alpha = N, \\ -\dfrac{\eta_0}{h_{\alpha+1}+h_\alpha}(\boldsymbol{u}_{\alpha+1}-\boldsymbol{u}_\alpha) & \text{for } \alpha = 1,\dots,N-1, \\ -\boldsymbol{\tau}_1 & \text{for } \alpha = 0, \end{cases} \tag{2.8}$$

where η_0 is the dynamic viscosity coefficient and the term for $\alpha = 0$ represents bottom friction. These viscous terms represent the vertical transfer of horizontal momentum between neighboring layers. In the general case, η_0 could depend on depth, turbulence, or sediment concentration (see, e.g., [22]), but here it is assumed constant for simplicity.

2.4. **Layer-wise effective tree density and porosity.** Let n_{t} denote the number of trees per unit length in the streamwise direction (as in the one-dimensional setup), A_{F} the forest cross-sectional area used to non-dimensionalize densities and d_α the mean diameter of the trees per layer. Then the effective tree density for layer α is taken as

$$n_{t,\alpha} = \frac{\bar{d}_\alpha m(\overline{c_{\mathrm{tr}}c_{\mathrm{le}}})_\alpha}{A_{\mathrm{F}}}, \tag{2.9}$$

where m is the density of trees and $(\overline{c_{\mathrm{tr}}c_{\mathrm{le}}})$ are the effect of branches and leafs (see Appendix A). Then, the layer porosity is defined by

$$\theta_\alpha \coloneqq 1 - \frac{n_{\mathrm{t},\alpha}\pi\bar{d}_\alpha^2}{4}. \tag{2.10}$$

The vectorial drag force per unit horizontal area acting on layer α is now given by

$$\boldsymbol{f}_{\mathrm{D},\alpha} = \frac{n_{\mathrm{t},\alpha}}{\theta_\alpha^2}\frac{1}{2}\rho C_{\mathrm{D},\alpha}A_{\mathrm{v},\alpha}\|\boldsymbol{u}_\alpha\|\boldsymbol{u}_\alpha = \frac{1}{2}\rho\frac{n_{t,\alpha}}{\theta_\alpha^2}C_{\mathrm{D}}(\mathrm{Re}_\alpha)(\overline{c_{\mathrm{tr}}c_{\mathrm{le}}})_\alpha\bar{d}_\alpha\|\boldsymbol{u}_\alpha\|\boldsymbol{u}_\alpha. \tag{2.11}$$

Similarly, if we assume radial symmetry of trunks, the inertia force per unit horizontal area is given by the following expression, where we adopt the calibration $C_{\mathrm{M},\alpha} = 2$ from [40]:

$$\boldsymbol{f}_{\mathrm{M},\alpha} = C_{\mathrm{M},\alpha}\frac{n_{\mathrm{t},\alpha}}{\theta_\alpha}h_\alpha A_{\mathrm{t},\alpha}\partial_t\boldsymbol{u}_\alpha = C_{\mathrm{M},\alpha}\frac{n_{\mathrm{t},\alpha}}{\theta_\alpha}h_\alpha\frac{\pi\bar{d}_\alpha^2}{4}\partial_t\boldsymbol{u}_\alpha. \tag{2.12}$$

3. Numerical implementation for the multi-layer tsunami model

To advance the multilayer model over one time step from t^ν to $t^{\nu+1} = t^\nu + \Delta t$, we adopt a fractional-step algorithm that separates the computation into three substeps: (i) a hydrostatic prediction, (ii) a friction and inertia correction, and (iii) a non-hydrostatic projection. These substeps correspond to intermediate times t^ν, $t^{\nu+1/3}$, $t^{\nu+2/3}$, and $t^{\nu+1}$. For simplicity, at each stage the respective preceding state is denoted by an asterisk $(*)$. Each stage preserves key physical constraints: positivity of the water depth, well-balancedness for the lake-at-rest state, and stability across wet/dry interfaces.

3.1. **Compact formulation.** The layer fluxes are defined component-wise as

$$\boldsymbol{F}_{\alpha,x}(\boldsymbol{W}_\alpha) = \begin{pmatrix} h_\alpha u_\alpha \\ h_\alpha u_\alpha^2 + \frac{1}{2} g h_\alpha^2 \\ h_\alpha u_\alpha v_\alpha \\ h_\alpha w_\alpha u_\alpha \end{pmatrix}, \qquad \boldsymbol{F}_{\alpha,y}(\boldsymbol{W}_\alpha) = \begin{pmatrix} h_\alpha v_\alpha \\ h_\alpha u_\alpha v_\alpha \\ h_\alpha v_\alpha^2 + \frac{1}{2} g h_\alpha^2 \\ h_\alpha w_\alpha v_\alpha \end{pmatrix},$$

so that the divergence term reads $\nabla \cdot \boldsymbol{F}_\alpha = \partial_x \boldsymbol{F}_{\alpha,x} + \partial_y \boldsymbol{F}_{\alpha,y}$, with interfacial coupling terms contained in $\boldsymbol{B}(\boldsymbol{W})$.

3.2. **Incorporation of inertia effects.** In tsunami propagation and run-up, high Froude number flows make the inertia force non-negligible. Following the approach in [12], we may incorporate these effects for each layer α by multiplying the system (1.2) by the 4×4 inertia matrix

$$\boldsymbol{\mathcal{M}}_\alpha = \begin{bmatrix} 1 & 0 & 0 & 0 \\ -k_{3,\alpha} u_\alpha & 1 + k_{3,\alpha} & 0 & 0 \\ -k_{3,\alpha} v_\alpha & 0 & 1 + k_{3,\alpha} & 0 \\ 0 & 0 & 0 & 1 \end{bmatrix}, \quad k_{3,\alpha} = C_{\mathrm{M}} \frac{n_{\mathrm{t},\alpha} \pi \overline{d}_\alpha^2}{4}.$$

The matrix $\boldsymbol{\mathcal{M}}_\alpha$ represents the added-inertia effect due to turbulent interactions within layer α. For the implementation of the FV method it is convenient to pre-multiply the flux terms by

$$\boldsymbol{\mathcal{C}}_\alpha \coloneqq \boldsymbol{\mathcal{M}}_\alpha^{-1} = \begin{bmatrix} 1 & 0 & 0 & 0 \\ \dfrac{k_{3,\alpha} u_\alpha}{1 + k_{3,\alpha}} & \dfrac{1}{1 + k_{3,\alpha}} & 0 & 0 \\ \dfrac{k_{3,\alpha} v_\alpha}{1 + k_{3,\alpha}} & 0 & \dfrac{1}{1 + k_{3,\alpha}} & 0 \\ 0 & 0 & 0 & 1 \end{bmatrix},$$

so that the inertia contributions are handled consistently in the flux computation. In other words, the original system for each layer is multiplied by $\boldsymbol{\mathcal{M}}_\alpha$ to include the inertia effects, and the FV discretization applies $\boldsymbol{\mathcal{C}}_\alpha$ to isolate the time derivatives and maintain a consistent conservative formulation.

3.3. **Hydrostatic predictor: path-conservative finite volume scheme.** At this stage, we advance the multilayer system under the hydrostatic assumption, setting all non-hydrostatic pressures to zero ($q = 0$). The corresponding hyperbolic part of the equations is discretized by means of a path-conservative FV scheme. This stage computes an intermediate state W_i^* that will later be corrected by the non-hydrostatic projection step.

The computational domain is partitioned into non-overlapping control volumes V_i with polygonal boundaries. For simplicity, we consider a Cartesian mesh, so that each cell V_i has area $|V_i| = \Delta x \Delta y$. Let $\mathcal{K}_i$ denote the set of indices of all cells V_k that share a common edge E_{ik} with V_i. The length of this edge is denoted by $|E_{ik}|$, and $\boldsymbol{\eta}_{ik} = (\eta_{x,ik}, \eta_{y,ik})^{\mathrm{T}}$ is the outward unit normal vector to E_{ik}, pointing from cell V_i toward cell V_k. The distance between the cell centers of V_i and V_k is written as d_{ik}. The marching formula of the FV method then reads

$$\boldsymbol{W}_i^* = \boldsymbol{W}_i^\nu - \frac{\Delta t}{|V_i|} \sum_{k \in \mathcal{K}_i} |E_{ik}| \mathcal{F}_{ik}(\boldsymbol{W}_i^\nu, \boldsymbol{W}_k^\nu, \boldsymbol{\eta}_{ik}) + \Delta t \boldsymbol{S}_i^{(\mathrm{f})}, \tag{3.1}$$

where $\boldsymbol{S}_i^{(\mathrm{f})}$ contains the hydrostatic source terms including the bed slope and vegetation contributions evaluated within cell V_i. For each edge E_{ik}, the numerical flux $\boldsymbol{\mathcal{F}}_{ik}(\boldsymbol{W}_i, \boldsymbol{W}_k, \boldsymbol{\eta}_{ik})$ approximates

the flux of the hyperbolic system in the direction of the interface normal $\boldsymbol{\eta}_{ik}$. The directionally projected flux is defined as

$$\boldsymbol{F}(\boldsymbol{W},\boldsymbol{\eta}) \coloneqq F_x(\boldsymbol{W})\boldsymbol{\eta}_x + F_y(\boldsymbol{W})\boldsymbol{\eta}_y,$$

where F_x and F_y are the physical flux functions effective in the x- and y-directions, respectively.

$$\boldsymbol{B}(\boldsymbol{W},\boldsymbol{\eta}) \coloneqq B_x(\boldsymbol{W})\boldsymbol{\eta}_x + B_y(\boldsymbol{W})\boldsymbol{\eta}_y,$$

where B_x and B_y denote the non-conservative matrices associated with the x- and y-directions, respectively, which is dimensionally consistent with the flux divergence terms in (3.1).

To compute $\boldsymbol{\mathcal{F}}_{ik}$, we employ a path-conservative HLL-type Riemann solver that also accounts for the non-conservative products $B_x(\boldsymbol{W})\partial_x\boldsymbol{W}$ and $B_y(\boldsymbol{W})\partial_y\boldsymbol{W}$ present in the multilayer formulation. For the edge between cells V_i and V_k the numerical flux is given by

$$\begin{aligned}\boldsymbol{\mathcal{F}}_{ik} = {}& \frac{1}{2}\boldsymbol{C}_{ik}\big(\boldsymbol{F}(\boldsymbol{W}_i,\boldsymbol{\eta}_{ik}) + \boldsymbol{F}(\boldsymbol{W}_k,\boldsymbol{\eta}_{ik})\big)\\ & - \frac{1}{2}\boldsymbol{C}_{ik}\Big(\alpha_{0,ik}(\boldsymbol{W}_k - \boldsymbol{W}_i)\\ & \qquad + \alpha_{1,ik}\big(\boldsymbol{F}(\boldsymbol{W}_k,\boldsymbol{\eta}_{ik}) - \boldsymbol{F}(\boldsymbol{W}_i,\boldsymbol{\eta}_{ik}) + \boldsymbol{\mathcal{B}}(\boldsymbol{W}_k,\boldsymbol{W}_i,\boldsymbol{\eta}_{ik})(\boldsymbol{W}_k - \boldsymbol{W}_i)\big)\Big),\end{aligned} \tag{3.2}$$

where the coefficients $\alpha_{0,ik}$ and $\alpha_{1,ik}$ are computed from the estimated minimum and maximum signal velocities $S_{\mathrm{L},ik}$ and $S_{\mathrm{R},ik}$ along the normal direction $\boldsymbol{\eta}_{ik}$:

$$\alpha_{0,ik} = \frac{S_{\mathrm{R},ik}|S_{\mathrm{L},ik}| - S_{\mathrm{L},ik}|S_{\mathrm{R},ik}|}{S_{\mathrm{R},ik} - S_{\mathrm{L},ik}}, \qquad \alpha_{1,ik} = \frac{|S_{\mathrm{R},ik}| - |S_{\mathrm{L},ik}|}{S_{\mathrm{R},ik} - S_{\mathrm{L},ik}}. \tag{3.3}$$

The operator $\boldsymbol{\mathcal{B}}(\boldsymbol{W}_k,\boldsymbol{W}_i,\boldsymbol{\eta}_{ik})$ represents the path integral of the non-conservative matrix along a straight segment joining $\boldsymbol{W}_i$ and $\boldsymbol{W}_k$ in the state space. This term guarantees the correct treatment of non-conservative products, which is essential for preserving the well-balanced property of the scheme.

The signal velocities $S_{\mathrm{L},ik}$ and $S_{\mathrm{R},ik}$ arising in (3.3) are estimated as in the standard HLL solver based on the layer-averaged velocities and the gravity-wave speed:

$$S_{\mathrm{L},ik} = \min_{1\le\alpha\le N}\big(u_i\eta_{x,ik} + v_i\eta_{y,ik} - \sqrt{gh_{\alpha,i}}\big), \qquad S_{\mathrm{R},ik} = \max_{1\le\alpha\le N}\big(u_k\eta_{x,ik} + v_k\eta_{y,ik} + \sqrt{gh_{\alpha,k}}\big).$$

This hydrostatic predictor stage produces the intermediate state $\boldsymbol{W}_i^*$, which is consistent with the hyperbolic dynamics of the multilayer model, maintains well-balancing for the still-water equilibrium, and preserves the positivity of the layer depths h_α. The correction due to non-hydrostatic pressure effects is subsequently applied during the projection step. The CFL condition ensuring stability is

$$\max_{i,k,l}\frac{|\lambda_{ik,l}|}{d_{ik}}\Delta t \le 1,$$

where d_{ik} is the distance between cell centers and $\lambda_{ik,l}$ is the l-th eigenvalue of the system matrix $\boldsymbol{A}(\boldsymbol{W}_i,\boldsymbol{\eta}_{ik})$ given by

$$\boldsymbol{A}(\boldsymbol{W},\boldsymbol{\eta}) = \left(\frac{\partial\boldsymbol{F}}{\partial\boldsymbol{W}}(\boldsymbol{W})\cdot\boldsymbol{\eta}\right) + \boldsymbol{B}(\boldsymbol{W},\boldsymbol{\eta}).$$

In practice, the eigenvalues $\lambda_{ik,l}$ are approximated by the characteristic wave speeds of a shallow water-type model defined at each layer. Instead of computing the full spectrum of $\boldsymbol{A}$, we use the

standard estimate of the propagation speeds. Consequently, the spectral radius required in the CFL condition is approximated by

$$\max_l |\lambda_{ik,l}| \;\approx\; \max_\alpha \left(|\boldsymbol{u}_{i,\alpha} \cdot \boldsymbol{\eta}_{ik}| + \sqrt{g h_i} \right).$$

3.4. **Hydrostatic reconstruction at an interface.** Consider an interface shared by a control volume V_i and one of its neighbouring cells V_k in a structured rectangular mesh. Without loss of generality, the index k refers to the neighbour located to the north or east of cell i. The free-surface elevations in the two cells are defined as $H_i \coloneqq h_i + z_{\mathrm{b},i}$ and $H_k \coloneqq h_k + z_{\mathrm{b},k}$, respectively, and the interface reference bed elevation is $z^*_{ik} \coloneqq \max\{z_{\mathrm{b},i}, z_{\mathrm{b},k}\}$. The hydrostatic reconstruction of the water depths across the interface between cells i and k is then given by

$$h^-_{ik} = \max\{H_i - z^*_{ik}, 0\}, \qquad h^+_{ik} = \max\{H_k - z^*_{ik}, 0\}. \tag{3.4}$$

For interfaces with neighbours to the west or south of cell i, the same expressions apply interchanges the roles of the "minus" and "plus" states.

Next, we reconstruct velocities and concentration consistently with the reconstructed depths. Assume that $\boldsymbol{u}_{\alpha,i} = (u_{\alpha,i}, v_{\alpha,i})$ is the horizontal velocity of layer α in cell i. We will use the same velocity components from the cell (i.e., hydrostatic reconstruction preserves the cell velocity), but the reconstructed momentum for each layer is scaled by the reconstructed depth:

$$\big(h\boldsymbol{u}_\alpha\big)^-_{ik} = h^-_{ik}\boldsymbol{u}_{\alpha,i}, \qquad \big(h\boldsymbol{u}_\alpha\big)^+_{ik} = h^+_{ik}\boldsymbol{u}_{\alpha,k}; \tag{3.5}$$

the same treatment is applied to hw_α. We collect the reconstructed quantities in the interfacial states

$$\boldsymbol{W}^-_{ik} \coloneqq \big(h^-_{ik}, \{h^-_{\alpha,ik}\boldsymbol{u}_{\alpha,i}, h^-_{\alpha,ik}w_{\alpha,i}\}_{\alpha=1}^N\big)^{\mathrm{T}}, \quad \boldsymbol{W}^+_{ik} \coloneqq \big(h^+_{ik}, \{h^+_{\alpha,ik}\boldsymbol{u}_{\alpha,k}, h^+_{\alpha,ik}w_{\alpha,k}\}_{\alpha=1}^N\big)^{\mathrm{T}}.$$

Using the hydrostatic reconstruction we enforce positivity and the well-balancing of the system, particularly in presence of dry fronts [3].

3.5. **Semi-implicit friction and inertia correction.** After the predictor step we apply a local implicit correction that incorporates the nonlinear drag and inertia effects. The hyperbolic step provides the intermediate state $\boldsymbol{W}^*$, and the corrected variables $\boldsymbol{W}^{\nu+1/3}$ are obtained by solving

$$\frac{1}{\Delta t}\big(\boldsymbol{W}^{\nu+1/3}_\alpha - \boldsymbol{W}^*_\alpha\big) = \boldsymbol{\mathcal{C}}_\alpha \boldsymbol{S}^{(\mathrm{f})}_\alpha\big(\boldsymbol{W}^{\nu+1/3}, \boldsymbol{W}^*\big), \quad \alpha = 1, \dots, N, \tag{3.6}$$

where $\boldsymbol{S}^{(\mathrm{f})}_\alpha$ contains the quadratic drag and bed friction terms, namely

$$\boldsymbol{S}^{(\mathrm{f})}_\alpha = \begin{pmatrix} 0 \\ -k_{2,\alpha}\|h_\alpha\boldsymbol{u}_\alpha\| h_\alpha\boldsymbol{u}_\alpha \\ 0 \end{pmatrix}, \qquad k_{2,\alpha} = \frac{C_{\mathrm{D},\alpha} d_\alpha n_{\mathrm{t},\alpha}}{2\theta_\alpha h_\alpha}.$$

To enhance stability, we evaluate the drag term in a semi-implicit form, namely

$$h_\alpha\boldsymbol{u}_\alpha|h_\alpha\boldsymbol{u}_\alpha| \approx (h_\alpha\boldsymbol{u}_\alpha)^{n+1}\|h_\alpha\boldsymbol{u}_\alpha\|^*,$$

so from (3.6) we get the layer update

$$\boldsymbol{W}^{\nu+1/3}_{\alpha,i} = \boldsymbol{N}_{\alpha,i}\boldsymbol{W}^*_{\alpha,i},$$

where we define

$$\boldsymbol{N}_{\alpha,i} \coloneqq \mathrm{diag}\left(1, \frac{1+k_{3,\alpha}}{1+k_{3,\alpha}+k_{2,\alpha}\|h_\alpha\boldsymbol{u}_\alpha\|\Delta t}, \frac{1+k_{3,\alpha}}{1+k_{3,\alpha}+k_{2,\alpha}\|h_\alpha\boldsymbol{u}_\alpha\|\Delta t}, 1\right).$$

3.6. **Adding viscosity and bottom friction.** At this stage, we have obtained all layer variables at time level $t^{\nu+1}$, denoted by the intermediate state $(\cdot)^*$, before accounting for viscous and bottom friction effects. Since these forces only modify the horizontal velocity field, the update is performed for $\boldsymbol{u}_\alpha$ while h_α is kept fixed. The correction step for each layer reads

$$h_\alpha \boldsymbol{u}_\alpha^{\nu+2/3} = h_\alpha \boldsymbol{u}_\alpha^* + \frac{\Delta t}{\theta_\alpha}\boldsymbol{K}_{\alpha-1/2}^{\nu+2/3} - \frac{\Delta t}{\theta_\alpha}\boldsymbol{K}_{\alpha+1/2}^{\nu+2/3}, \quad \alpha = 1,\dots,N, \tag{3.7}$$

where the interlayer viscous terms $\boldsymbol{K}_{\alpha\pm1/2}$, the bottom friction $\boldsymbol{K}_{-1/2} = -\boldsymbol{\tau}_1$, and $\boldsymbol{K}_{N+1/2} = \boldsymbol{0}$ are defined in (2.8). Substituting the definitions of $\boldsymbol{K}_{\alpha\pm1/2}$ and $\boldsymbol{\tau}_1$, we obtain the following implicit relations for the corrected velocities $\boldsymbol{u}_\alpha^{\nu+2/3}$, $\alpha = 1,\dots,N$:

$$\begin{aligned}
h_1\boldsymbol{u}_1^{\nu+2/3} &= h_1\boldsymbol{u}_1^* - \Delta t k_1 \|h_1\boldsymbol{u}_1^*\| h_1\boldsymbol{u}_1^{\nu+2/3} + \frac{\Delta t\eta_0}{2\theta_1 h_1}\big(\boldsymbol{u}_2^{\nu+2/3} - \boldsymbol{u}_1^{\nu+2/3}\big),\\
h_\alpha\boldsymbol{u}_\alpha^{\nu+2/3} &= h_\alpha\boldsymbol{u}_\alpha^* - \frac{\Delta t\eta_0}{2\theta_\alpha h_\alpha}\big(\boldsymbol{u}_\alpha^{\nu+2/3} - \boldsymbol{u}_{\alpha-1}^{\nu+2/3}\big) + \frac{\Delta t\eta_0}{2\theta_\alpha h_\alpha}\big(\boldsymbol{u}_{\alpha+1}^{\nu+2/3} - \boldsymbol{u}_\alpha^{\nu+2/3}\big), \quad \alpha = 2,\dots,N-1,\\
h_N\boldsymbol{u}_N^{\nu+2/3} &= h_N\boldsymbol{u}_N^* - \frac{\Delta t\eta_0}{2\theta_N h_N}\big(\boldsymbol{u}_N^{\nu+2/3} - \boldsymbol{u}_{N-1}^{\nu+2/3}\big).
\end{aligned}$$

This system can be rewritten as

$$\begin{aligned}
\left(1 + \frac{\eta_0\Delta t}{2\theta_1 h_1^2} + \Delta t k_1\|h_1\boldsymbol{u}_1^*\|\right)h_1\boldsymbol{u}_1^{\nu+2/3} - \frac{\eta_0\Delta t}{2\theta_1 h_1^2}h_1\boldsymbol{u}_2^{\nu+2/3} &= h_1\boldsymbol{u}_1^*,\\
\left(1 + \frac{\eta_0\Delta t}{\theta_\alpha h_\alpha^2}\right)h_\alpha\boldsymbol{u}_\alpha^{\nu+2/3} - \frac{\eta_0\Delta t}{2\theta_\alpha h_\alpha^2}h_\alpha\big(\boldsymbol{u}_{\alpha-1}^{\nu+2/3} + \boldsymbol{u}_{\alpha+1}^{\nu+2/3}\big) &= h_\alpha\boldsymbol{u}_\alpha^*, \quad \alpha = 2,\dots,N-1,\\
\left(1 + \frac{\eta_0\Delta t}{2\theta_N h_N^2}\right)h_N\boldsymbol{u}_N^{\nu+2/3} - \frac{\eta_0\Delta t}{2\theta_N h_N^2}h_N\boldsymbol{u}_{N-1}^{\nu+2/3} &= h_N\boldsymbol{u}_N^*.
\end{aligned} \tag{3.8}$$

The coefficient matrix of the tridiagonal linear system (3.8) is symmetric and strictly diagonally dominant, and it is solved efficiently at each time step by a Thomas algorithm. Since each horizontal velocity component (u_α, v_α) evolves independently in this step, the same tridiagonal system is solved twice, once for each velocity component.

3.7. **Non-hydrostatic projection.** The non-hydrostatic variables q_α (and the interface pressures $q_{\alpha\pm1/2}$) are not advanced through hyperbolic transport equations. Instead, they are obtained by enforcing the incompressibility or kinematic constraint (2.5) at the new time step. This procedure leads to an elliptic (Poisson-like) problem for the pressure corrections which is solved during the projection step. The projection approach introduced in [12] extends naturally to two dimensions, with the elliptic operator incorporating spatially variable coefficients that depend on the layer thickness h_α, the porosity θ_α, and the geometric effects associated with the bottom topography ∇z_b.

The intermediate solution $\boldsymbol{W}^*$ is corrected by projecting the non-hydrostatic pressure field. For each layer α, the intermediate velocities $\boldsymbol{u}_\alpha^*$ and w_α^* are updated according to the pressure gradients obtained from the solution of the elliptic system. It is worth noting that since the mass conservation equation for h_α does not depend on the non-hydrostatic pressure, the layer thickness remains unchanged during this projection step, that is,

$$h_\alpha^{\nu+1} = h_\alpha^*, \quad \alpha = 1,\dots,N.$$

The correction is thus applied exclusively to the velocity components, which ensures that the final solution satisfies the discrete incompressibility constraint at time level $\nu+1$. The correction is

computed from

$$h_\alpha^{\nu+1}\boldsymbol{u}_\alpha^{\nu+1} = h_\alpha^*\boldsymbol{u}_\alpha^* - f_\alpha^*\Delta t\Big(\frac{1}{2}\nabla\big(h_\alpha^{\nu+1}q_{\alpha-1/2}^{\nu+1} + h_\alpha^{\nu+1}q_{\alpha+1/2}^{\nu+1}\big) + q_{\alpha-1/2}^{\nu+1}\nabla z_{\alpha-1/2}^{\nu+1} - q_{\alpha+1/2}^{\nu+1}\nabla z_{\alpha+1/2}^{\nu+1}\Big) \tag{3.9}$$

with

$$f_\alpha = \frac{\theta_\alpha}{1 + k_{3,\alpha} + k_{2,\alpha}\|\boldsymbol{u}_\alpha\|\Delta t},$$

and where $q_{\alpha\pm1/2}$ denotes the non-hydrostatic pressure at the interface between layers α and $\alpha\pm1/2$. For the vertical velocity we have

$$h_\alpha^{\nu+1}w_\alpha^{\nu+1} = h_\alpha^*w_\alpha^* - \Delta t q_{\alpha+1/2}^{\nu+1} + \Delta t q_{\alpha-1/2}^{\nu+1}. \tag{3.10}$$

On the other hand, multiplying the incompressibility constraint (2.5) by h_α and applying it to each layer, for the bottom layer ($\alpha = 1$) we obtain

$$-h_1\nabla\cdot(h_1\boldsymbol{u}_1) + 2(\nabla z_1)\cdot h_1\boldsymbol{u}_1 - 2h_1w_1 = 0, \tag{3.11}$$

while for the higher layers ($\alpha = 2,\dots,N$), subtracting the condition at layer $\alpha-1$ from that at layer α and regrouping terms gives, since all layers share the same thickness,

$$-h_\alpha\nabla\cdot(h_\alpha\boldsymbol{u}_\alpha) - h_\alpha\nabla\cdot(h_\alpha\boldsymbol{u}_{\alpha-1}) + 2h_\alpha\boldsymbol{u}_\alpha\cdot\nabla z_\alpha - 2h_\alpha\boldsymbol{u}_{\alpha-1}\cdot\nabla z_{\alpha-1} - 2h_\alpha w_\alpha + 2h_\alpha w_{\alpha-1} = 0. \tag{3.12}$$

Replacing (3.9) and (3.10) in the incompressibility conditions (3.11)–(3.12) we get a linear system of equations for the unknown interface pressures $q_{\alpha+1/2}$. For simplicity, in what follows we denote $h_\alpha^{n+1} = h_\alpha^*$ and $z_\alpha^{n+1} = z_\alpha^*$ simply as h_α and z_α, respectively. We recall that $\nabla = (\partial_x, \partial_y)$ denotes the continuous horizontal gradient operator:

$$\begin{aligned}
&h_\alpha\nabla\cdot\left(f_\alpha^*\Delta t\left(\frac{1}{2}\nabla(h_\alpha q_{\alpha-1/2}^{\nu+1}) + \frac{1}{2}\nabla(h_\alpha q_{\alpha+1/2}^{\nu+1}) + q_{\alpha-1/2}^{\nu+1}\nabla z_{\alpha-1/2} - q_{\alpha+1/2}^{\nu+1}\nabla z_{\alpha+1/2}\right)\right)\\
&+ h_\alpha\nabla\cdot\left(f_{\alpha-1}^*\Delta t\left(\frac{1}{2}\nabla(h_\alpha q_{\alpha-3/2}^{\nu+1}) + \frac{1}{2}\nabla(h_\alpha q_{\alpha-1/2}^{\nu+1}) + q_{\alpha-3/2}^{\nu+1}\nabla z_{\alpha-3/2} - q_{\alpha-1/2}^{\nu+1}\nabla z_{\alpha-1/2}\right)\right)\\
&- 2f_\alpha^*\Delta t\left(\frac{1}{2}\nabla(h_\alpha q_{\alpha-1/2}^{\nu+1}) + \frac{1}{2}\nabla(h_\alpha q_{\alpha+1/2}^{\nu+1}) + q_{\alpha-1/2}^{\nu+1}\nabla z_{\alpha-1/2} - q_{\alpha+1/2}^{\nu+1}\nabla z_{\alpha+1/2}\right)\cdot\nabla z_\alpha\\
&+ 2f_{\alpha-1}^*\Delta t\left(\frac{1}{2}\nabla(h_\alpha q_{\alpha-3/2}^{\nu+1}) + \frac{1}{2}\nabla(h_\alpha q_{\alpha-1/2}^{\nu+1}) + q_{\alpha-3/2}^{\nu+1}\nabla z_{\alpha-3/2} - q_{\alpha-1/2}^{\nu+1}\nabla z_{\alpha-1/2}\right)\cdot\nabla z_{\alpha-1}\\
&- 2\Delta t\big(q_{\alpha+1/2}^{\nu+1} - 2q_{\alpha-1/2}^{\nu+1} + q_{\alpha-3/2}^{\nu+1}\big)\\
&= h_\alpha\nabla\cdot(h_\alpha\boldsymbol{u}_\alpha^*) + h_\alpha\nabla\cdot(h_\alpha\boldsymbol{u}_{\alpha-1}^*) - 2h_\alpha\boldsymbol{u}_\alpha^*\cdot\nabla z_\alpha + 2h_\alpha\boldsymbol{u}_{\alpha-1}^*\cdot\nabla z_{\alpha-1} + 2(h_\alpha w_\alpha^* - h_\alpha w_{\alpha-1}^*).
\end{aligned} \tag{3.13}$$

In matrix form, this system resembles a discrete Poisson problem that links all layers through the vertical fluxes. The projection step is implemented on a structured Cartesian mesh using a staggered arrangement of variables following the classical Arakawa C-grid configuration [21]. Scalar quantities h_α and the horizontal discharges $h_\alpha\boldsymbol{u}_\alpha$ are stored at cell centers (x_i, y_j), while the interface pressures $q_{\alpha\pm1/2}$ and vertical velocities w_α are defined at cell corners $(x_{i+1/2}, y_{j+1/2})$. This layout ensures a consistent discretization of the gradient and divergence operators appearing in the projection step. Spatial derivatives are evaluated using second-order centered finite differences, with quantities required at corner nodes obtained by arithmetic averaging of the four surrounding cell-centered values. For further details on the staggered discretization and the finite-difference

operators we refer to [21]. The fully discrete linear system to be solved for the unknown interface pressures $\boldsymbol{q}^{\nu+1} = (q_{1/2}^{\nu+1}, q_{3/2}^{\nu+1}, \dots, q_{N+1/2}^{\nu+1})^{\mathrm{T}}$ at each corner node $(x_{i+1/2}, y_{j+1/2})$ takes the form

$$\boldsymbol{M}\boldsymbol{q}^{\nu+1} = \boldsymbol{P}^*, \tag{3.14}$$

where $\boldsymbol{M}$ is a sparse matrix with at most five nonzero entries per row, and $\boldsymbol{P}^*$ collects all right-hand side terms evaluated at the intermediate state $\boldsymbol{W}^*$ (see the right-hand side of the incompressibility conditions (3.13)). Specifically,

$$\begin{aligned} P^* = {} & M_{p,p} q_{\alpha-1/2,i+1/2,j+1/2} + M_{p,p_{\mathrm{E}}} q_{\alpha-1/2,i+3/2,j+1/2} + M_{p,p_{\mathrm{W}}} q_{\alpha-1/2,i-1/2,j+1/2} \\ & + M_{p,p_{\mathrm{N}}} q_{\alpha-1/2,i+1/2,j+3/2} + M_{p,p_{\mathrm{S}}} q_{\alpha-1/2,i+1/2,j-1/2}. \end{aligned}$$

The subscripts E, W, N, and S within the coefficients $M_{p,p}$, $M_{p,p_{\mathrm{E}}}$, $M_{p,p_{\mathrm{W}}}$, $M_{p,p_{\mathrm{N}}}$, and $M_{p,p_{\mathrm{S}}}$ indicate the adjacent control volumes in the positive x-direction (east), negative x-direction (west), positive y-direction (north), and negative y-direction (south). Thus, the discrete operator represents a five-point stencil coupling the pressure unknown q at the cell corner with its four immediate horizontal neighbours.

Boundary conditions for the pressure system follow the approach of [21], extended here to each interface pressure $q_{\alpha+1/2}$, $\alpha = 1, \dots, N$. At solid wall boundaries, a homogeneous Neumann condition is imposed, implemented via ghost cells whose pressure values are extrapolated from the adjacent interior cells, which is equivalent to enforcing

$$\nabla q_{\alpha+1/2} \cdot \boldsymbol{n} = 0 \quad \text{on } \partial\Omega.$$

At open or absorbing boundaries, the non-hydrostatic pressure is relaxed toward zero through a sponge layer that drives $q_{\alpha+1/2}$ to zero smoothly so that outgoing waves leave the domain without spurious reflections [21]. Together, these conditions close the system (3.14).

All coefficients are evaluated at the edge location $(x_{i+1/2}, y_{j+1/2})$ unless otherwise noted. We denote by $f_{\alpha,i+1/2,j+1/2}$ the interpolation of f_α to the corner $(x_{i+1/2}, y_{j+1/2})$, which is computed as the arithmetic mean of the two cell-centred values sharing that edge, i.e.,

$$f_{\alpha,i+1/2,j+1/2} = \frac{1}{2}(f_{\alpha,i,j+1/2} + f_{\alpha,i+1,j+1/2}),$$

and analogously in the y-direction for the north/south edges, and similarly for $h_{i+1/2,j+1/2}$. We also introduce the auxiliary function $\boldsymbol{\phi}$

$$\boldsymbol{\phi}_\alpha = 2N\nabla\left(z_{\alpha-1/2} + \frac{h_\alpha}{2}\right) = \left(\phi_\alpha^{(x)}, \phi_\alpha^{(y)}\right).$$

We use the notation $|\boldsymbol{\phi}_\alpha|^2 \coloneqq (\phi_\alpha^{(x)})^2 + (\phi_\alpha^{(y)})^2$, and it is assumed that the spatial derivatives at the point $(x_{i+1/2}, y_{j+1/2})$ are approximated by suitable central differences. Precisely, we introduce the notation

$$\begin{aligned} \mathrm{D}_x\varphi_{i+1/2,j+1/2} &\coloneqq \frac{\varphi_{i+1,j+1/2} - \varphi_{i,j+1/2}}{\Delta x} \approx (\partial_x\varphi)(x_{i+1/2}, y_{j+1/2}), \\ \mathrm{D}_y\varphi_{i+1/2,j+1/2} &\coloneqq \frac{\varphi_{i+1/2,j+1} - \varphi_{i+1/2,j}}{\Delta y} \approx (\partial_y\varphi)(x_{i+1/2}, y_{j+1/2}), \end{aligned}$$

where φ denotes the interpolated quantity.

The nonzero coefficients of $\mathbf{M}$ in (3.14) are given explicitly below.

$$
\begin{aligned}
M_{p,p} = {} & 8N^2 + f_{\alpha,i+1/2,j+1/2}|\boldsymbol{\phi}_{\alpha,i+1/2,j+1/2}|^2 + f_{\alpha-1,i+1/2,j+1/2}|\boldsymbol{\phi}_{\alpha-1,i+1/2,j+1/2}|^2 \\
& - h_{i+1/2,j+1/2}\mathrm{D}_x\big(f_{\alpha,i+1/2,j+1/2}\phi^{(x)}_{\alpha,i+1/2,j+1/2}\big) \\
& + h_{i+1/2,j+1/2}\mathrm{D}_x\big(f_{\alpha-1,i+1/2,j+1/2}\phi^{(x)}_{\alpha-1,i+1/2,j+1/2}\big) \\
& - h_{i+1/2,j+1/2}\mathrm{D}_y\big(f_{\alpha,i+1/2,j+1/2}\phi^{(y)}_{\alpha,i+1/2,j+1/2}\big) \\
& + h_{i+1/2,j+1/2}\mathrm{D}_y\big(f_{\alpha-1,i+1/2,j+1/2}\phi^{(y)}_{\alpha-1,i+1/2,j+1/2}\big) \\
& + \left(\frac{2}{\Delta x^2} + \frac{2}{\Delta y^2}\right) h^2_{i+1/2,j+1/2}\big(f_{\alpha,i+1/2,j+1/2} + f_{\alpha-1,i+1/2,j+1/2}\big),
\end{aligned}
\tag{3.15}
$$

the coefficients in x-direction

$$
\begin{aligned}
M_{p,p_{\mathrm{E}}} = {} & -\frac{1}{2\Delta x}\big(h_{i+1/2,j+1/2}\mathrm{D}_x(f_{\alpha,i+1/2,j+1/2}h_{i+1/2,j+1/2}) \\
& \qquad + h_{i+1/2,j+1/2}\mathrm{D}_x(f_{\alpha-1,i+1/2,j+1/2}h_{i+1/2,j+1/2})\big) \\
& - \frac{1}{\Delta x^2} h^2_{i+1/2,j+1/2}(f_{\alpha,i+1/2,j+1/2} + f_{\alpha-1,i+1/2,j+1/2}), \\
M_{p,p_{\mathrm{W}}} = {} & +\frac{1}{2\Delta x}\big(h_{i+1/2,j+1/2}\mathrm{D}_x(f_{\alpha,i+1/2,j+1/2}h_{i+1/2,j+1/2}) \\
& \qquad + h_{i+1/2,j+1/2}\mathrm{D}_x(f_{\alpha-1,i+1/2,j+1/2}h_{i+1/2,j+1/2})\big) \\
& - \frac{1}{\Delta x^2} h^2_{i+1/2,j+1/2}(f_{\alpha,i+1/2,j+1/2} + f_{\alpha-1,i+1/2,j+1/2})
\end{aligned}
\tag{3.16}
$$

and the analogous coefficients in y-direction

$$
\begin{aligned}
M_{p,p_{\mathrm{N}}} = {} & -\frac{1}{2\Delta y}\big(h_{i+1/2,j+1/2}\mathrm{D}_y(f_{\alpha,i+1/2,j+1/2}h_{i+1/2,j+1/2}) \\
& \qquad + h_{i+1/2,j+1/2}\mathrm{D}_y(f_{\alpha-1,i+1/2,j+1/2}h_{i+1/2,j+1/2})\big) \\
& - \frac{1}{\Delta y^2} h^2_{i+1/2,j+1/2}(f_{\alpha,i+1/2,j+1/2} + f_{\alpha-1,i+1/2,j+1/2}), \\
M_{p,p_{\mathrm{S}}} = {} & +\frac{1}{2\Delta y}\big(h_{i+1/2,j+1/2}\mathrm{D}_y(f_{\alpha,i+1/2,j+1/2}h_{i+1/2,j+1/2}) \\
& \qquad + h_{i+1/2,j+1/2}\mathrm{D}_y(f_{\alpha-1,i+1/2,j+1/2}h_{i+1/2,j+1/2})\big) \\
& - \frac{1}{\Delta y^2} h^2_{i+1/2,j+1/2}(f_{\alpha,i+1/2,j+1/2} + f_{\alpha-1,i+1/2,j+1/2}).
\end{aligned}
\tag{3.17}
$$

Finally, $M_{p,q} = 0$ for all other columns, so each row has at most five nonzero entries.

The system matrix is similar to the one introduced in [12] in the one-dimensional context. To obtain the solution, we employ an iterative algorithm (e.g., a Gauss–Seidel relaxation) until the residual of the incompressibility constraints falls below a prescribed tolerance (10^{-6}).

Once the pressure field is computed, we return to (3.9)–(3.10) and correct the velocities accordingly, evaluating $q_{\alpha+1/2}$ with the obtained values.

3.8. **Summary of algorithm per time step.** The complete scheme described in the present section advances the solution from t^ν to $t^{\nu+1} = t^\nu + \Delta t$ as summarized in Algorithm 1.

Algorithm 1: Time stepping for the 2D multilayer non-hydrostatic tsunami–forest model

Input: $\boldsymbol{W}^\nu = (h_\alpha^\nu, h_\alpha^\nu \boldsymbol{u}_\alpha^\nu, h_\alpha^\nu w_\alpha^\nu)_{\alpha=1}^N$, bathymetry $z_\mathrm{b} = z_\mathrm{b}(x,y)$, vegetation parameters $(n_{\mathrm{t},\alpha}, \bar{d}_\alpha, \theta_\alpha)_{\alpha=1}^N$, time step Δt satisfying the CFL condition.

Output: $\boldsymbol{W}^{\nu+1} = (h_\alpha^{\nu+1}, h_\alpha^{\nu+1}\boldsymbol{u}_\alpha^{\nu+1}, h_\alpha^{\nu+1} w_\alpha^{\nu+1})_{\alpha=1}^N$

`// Step 1 | Hydrostatic predictor`

1. Hydrostatic predictor. Set $q_{\alpha\pm1/2} = 0$ and advance the system (1.2) via the path-conservative HLL flux (3.2) with hydrostatic reconstruction (3.4), (3.5),

$$\boldsymbol{W}_{\alpha,i}^{(1)} = \boldsymbol{W}_{\alpha,i}^\nu - \frac{\Delta t}{|V_i|} \sum_{k\in\mathcal{K}_i} |E_{ik}| \boldsymbol{\mathcal{F}}_{ik}(\boldsymbol{W}_i^\nu, \boldsymbol{W}_k^\nu, \boldsymbol{\eta}_{ik}) + \Delta t \boldsymbol{S}_i^{(\mathrm{f})},$$

to obtain $\boldsymbol{W}^{(1)}$. from $\boldsymbol{W}^\nu$.

`// Step 2 | Vegetation and friction corrections`

2. Inertia and drag correction. Following the approach of Section 3.5 we apply the semi-implicit drag correction (3.6) to obtain

$$\boldsymbol{W}_{\alpha,i}^{(\nu+1/3)} = \boldsymbol{N}_{\alpha,i} \boldsymbol{W}_{\alpha,i}^{(1)},$$

where

$$\boldsymbol{N}_{\alpha,i} := \mathrm{diag}\left(1,\ \frac{1+k_{3,\alpha}}{1+k_{3,\alpha}+k_{2,\alpha}\|h_\alpha \boldsymbol{u}_\alpha\|\Delta t},\ \frac{1+k_{3,\alpha}}{1+k_{3,\alpha}+k_{2,\alpha}\|h_\alpha \boldsymbol{u}_\alpha\|\Delta t},\ 1\right).$$

3. Viscosity and inter-layer friction. Solve the symmetric tridiagonal system (3.8), independently for each component (u_α, v_α) and with $\boldsymbol{u}_\alpha^*$ replaced by $\boldsymbol{u}_\alpha^{\nu+1/3}$, for instanxce by the Thomas algorithm, to obtain $\boldsymbol{u}_\alpha^{\nu+2/3}$.

`// Step 3 | Non-hydrostatic projection`

4. Non-hydrostatic projection Set $h_\alpha^{\nu+1} = h_\alpha^*$ and:

(a) Solve the pressure system (3.14), with coefficients (3.15)–(3.17), for $\boldsymbol{q}^{\nu+1} = (q_{1/2}^{\nu+1}, \ldots, q_{N+1/2}^{\nu+1})^\mathrm{T}$ via Gauss–Seidel iteration until $\|\boldsymbol{P}^* - \mathbf{M}\boldsymbol{q}^{\nu+1}\|_\infty < 10^{-6}$.

(b) Correct horizontal and vertical velocities via (3.9)–(3.10):

$$\begin{aligned} h_\alpha^{\nu+1}\boldsymbol{u}_\alpha^{\nu+1} &= h_\alpha^*\boldsymbol{u}_\alpha^* - f_\alpha^*\Delta t\Big(\tfrac{1}{2}\nabla\big(h_\alpha^{\nu+1}(q_{\alpha-1/2}^{\nu+1} + q_{\alpha+1/2}^{\nu+1})\big) \\ &\qquad + q_{\alpha-1/2}^{\nu+1}\nabla z_{\alpha-1/2}^{\nu+1} - q_{\alpha+1/2}^{\nu+1}\nabla z_{\alpha+1/2}^{\nu+1}\Big), \\ h_\alpha^{\nu+1} w_\alpha^{\nu+1} &= h_\alpha^* w_\alpha^* - \Delta t q_{\alpha+1/2}^{\nu+1} + \Delta t q_{\alpha-1/2}^{\nu+1}. \end{aligned}$$

Now $\boldsymbol{W}^{\nu+1} = (h_\alpha^{\nu+1}, h_\alpha^{\nu+1}\boldsymbol{u}_\alpha^{\nu+1}, h_\alpha^{\nu+1} w_\alpha^{\nu+1})_{\alpha=1}^N$ is the sought output.

`// Step 4 | Time step control`

5. CFL update. Compute $\Delta t^{\nu+1}$ from $\max\limits_{i,k,\ell} \dfrac{|\lambda_{ik,\ell}|}{d_{ik}} \Delta t \le 1$ and set $t^{\nu+1} := t^\nu + \Delta t$.

4. Numerical examples

4.1. **Example 1: convergence test.** To assess the convergence of the numerical scheme we record the history of approximate L^1 errors for the case of the interaction of a solitary wave with a conical island (this configuration is described in detail in Section 4.3). The computational domain and physical parameters are identical to those of the reference solution, with the obvious exception of the grid resolution which is systematically refined. Five uniform square grids of $\mathcal{N} \times \mathcal{N}$ cells with $\mathcal{N} = 100$, 200, 400, 800, and 3200 are considered, where the numerical solution on the finest grid ($\mathcal{N} = 3200$) is taken as the reference solution, and the L^1 norm of the error is computed for the

TABLE 1. Example 1 (convergence test against reference solution on a 3200×3200 grid at simulated time $t = 50\,\mathrm{s}$): approximate L^1 errors for the free surface η, the horizontal velocities u and v, and the vertical velocity w.

$\mathcal{N} \times \mathcal{N}$	Δx	L^1 error			
		η	u	v	w
100×100	0.2800	2.55×10^{-3}	2.88×10^{-2}	1.70×10^{-2}	2.07×10^{-3}
200×200	0.1400	1.82×10^{-3}	1.51×10^{-2}	8.91×10^{-3}	1.26×10^{-3}
400×400	0.0700	1.13×10^{-3}	1.16×10^{-2}	6.11×10^{-3}	1.22×10^{-3}
800×800	0.0350	7.49×10^{-4}	5.63×10^{-3}	3.50×10^{-3}	8.23×10^{-4}
Overall order (LS)		0.60	0.74	0.74	0.40

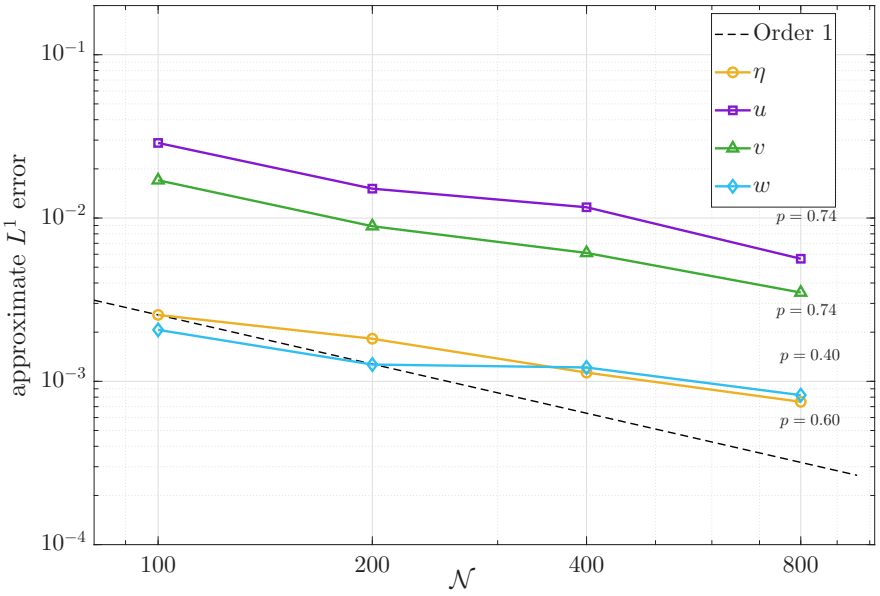

FIGURE 2. Example 1 (convergence test against reference solution on a 3200×3200 grid at simulated time $t = 50\,\mathrm{s}$): approximate L^1 errors at simulated time $t = 50\,\mathrm{s}$ for the free-surface elevation η, horizontal velocity components u and v, and vertical velocity w, obtained from the test on the conical island case (Section 4.3). Dashed and dotted lines indicate first- and second-order reference slopes, respectively.

free-surface elevation η, the horizontal velocity components u and v, and the vertical velocity w at simulated time $t = 50\,\mathrm{s}$. The results are presented in Table 1 and Figure 2, showing that the scheme achieves convergence rates smaller than one (with overall rates of 0.60, 0.74, and 0.74 for η, u, and v, respectively). The vertical velocity w exhibits a lower convergence rate of 0.40, probably due to increased sensitivity to the accumulated truncation error in the projection method.

4.2. **Examples 2 to 4: numerical tests based on laboratory experiments by Iimura and Tanaka [27].** The numerical tests presented here are based on the laboratory experiments by Iimura and Tanaka [27], who investigated tsunami–vegetation interactions by using a laboratory

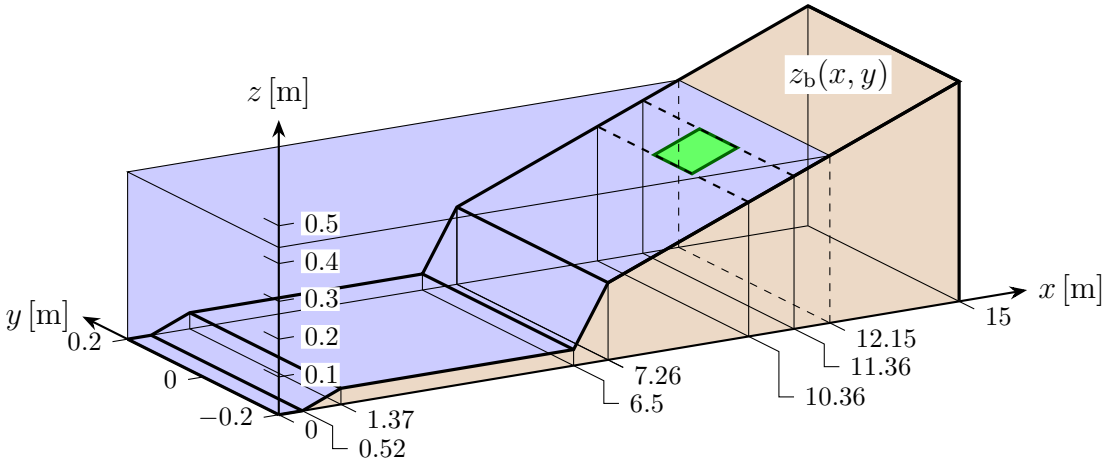

FIGURE 3. Examples 2 and 3: schematic of the experimental used in [27]. The steepness of the inclined portions of $z_b(x,y)$, for fixed y, is 1:20 for $x \in [0.52\,\text{m}, 1.37\,\text{m}]$, 1:4.5 for $x \in [6.5\,\text{m}, 7.26\,\text{m}]$, and 1:20.5 for $x \in [7.26\,\text{m}, 15\,\text{m}]$. The dashed lines enclose the forest area stretching over the full width of the channel for Example 2, and the green area denotes an inclined rectangle corresponding to the assumed vegetation area of Example 3. Notice that different scales are used for the x-, y- and z-axes.

channel at 1:100 scale. This configuration was previously used in one-dimensional multilayer simulations [12] to validate the LDNH$_0$ model against measured water levels and drag forces. Here, we extend the approach to two horizontal dimensions to analyze lateral effects on tsunami attenuation and flow variability induced by vegetation.

4.2.1. *Experimental setup, vegetation parameters and wave generation.* The experimental setup consists of a 15 m-long and 0.4 m-wide flume with a sloping bottom representing a beach (Figure 3). A wave-making plate at $x = 0\,\text{m}$ generates a solitary wave of amplitude $\eta_0 = 3.14$ cm over still water depth $h_0 = 0.4\,\text{m}$. Vegetation is represented by arrays of vertical cylinders ($d = 5\,\text{mm}$) arranged between $x = 10.36\,\text{m}$ and $x = 11.36\,\text{m}$, forming forest patches of varying density. We here select Case 3 of the 15 cases studied in [27]. For this case, the forest is uniform and the spacing between neighbouring trees is $D_b = 50\,\text{mm}$. The tree density, in trees per square meter, is $n_t = 577.5\,\text{m}^{-2}$. The solitary wave generated by the piston follows the Rayleigh profile [30]:

$$\eta(x,0) = \eta_0 \text{sech}^2(\beta x), \qquad \beta = \sqrt{\frac{3\eta_0}{4h_0^2(h_0+\eta_0)}}, \qquad u(x,0) = c\frac{\eta(x,0)}{h(x,0)}, \quad c = \sqrt{g(h_0+\eta_0)}. \tag{4.1}$$

4.2.2. *Computational domain and boundary conditions.* The full flume ($15\,\text{m} \times 0.4\,\text{m}$) is discretized with a uniform Cartesian mesh with $\Delta x = \Delta y = 0.02\,\text{m}$. The inlet imposes the solitary wave of (4.1), the outlet uses a transmissive condition to prevent reflections, and lateral walls are treated as slip boundaries.

4.2.3. *Example 2: calibration results.* As a first validation, we reproduce Case 3, of Iimura et al. [27] experiment, described at the beginning of Section 4, corresponding to a uniform forest. Figure 4 compares the simulated free-surface elevation at the downstream edge of the vegetation with the experimental data. The simulation accurately reproduces the wave amplitude, shape, and arrival

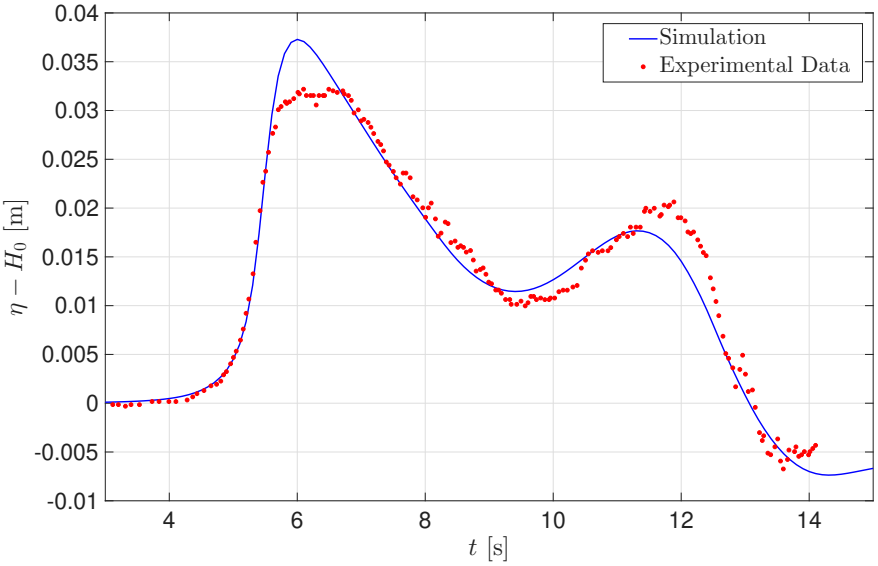

FIGURE 4. Example 2: Temporal evolution of η in Case 3 of [27] at the downstream end of the vegetation ($x = 11.36$ m), with $H_0 = 0.44$ m representing the water level at rest.

time, demonstrating that the model correctly captures the interaction between the solitary wave and the vegetation array. This single calibration test confirms that the numerical framework resolves the key hydrodynamic processes, including wave attenuation, flow redistribution. Having established this baseline, the model will be used in subsequent simulations to systematically investigate how different forest configurations influence tsunami propagation and flow dynamics.

4.2.4. *Example 3: partial forest configuration: central patch.* To investigate the influence of lateral forest distribution, we consider a variation of Case 3 in which the vegetation is confined to the central portion of the flume. In this configuration, the forest occupies only the region $y \in [-0.05, 0.05]$ m in the transverse direction, which spans the full channel width of $[-0.2, 0.2]$ m. Also we will consider 10 layers case in order to also study the verticality of the test.

This setup allows us to investigate how the partial lateral coverage of the forest modifies tsunami propagation, wave attenuation, and flow redistribution. By comparing this configuration with the full-width forest of Case 3, we can isolate the influence of lateral variability and assess how concentrated vegetation patches affect both the amplitude and the spatial structure of the water surface, including potential lateral flow around the vegetation.

As shown in Figure 5, the incoming wave reaches the upstream edge of the forest ($x = 11$ m) at approximately $t = 6$ s, where the vegetation partially blocks its propagation. Along the flume sides, outside the vegetated region, the wave advances freely, illustrating how lateral confinement of the forest redistributes the flow. When the backflow develops after reflection from downstream, the vegetation again exerts a damping effect, reducing both the velocity and surface elevation of the returning wave.

Figure 6 presents the corresponding horizontal velocity field $\boldsymbol{u} = (u, v)^{\mathrm{T}}$ at two characteristic stages. At $t = 6$ s, as the wave front impacts the forest, the vegetation generates a strong resistance that decelerates the flow within the canopy and increases velocity upstream of it. This partial

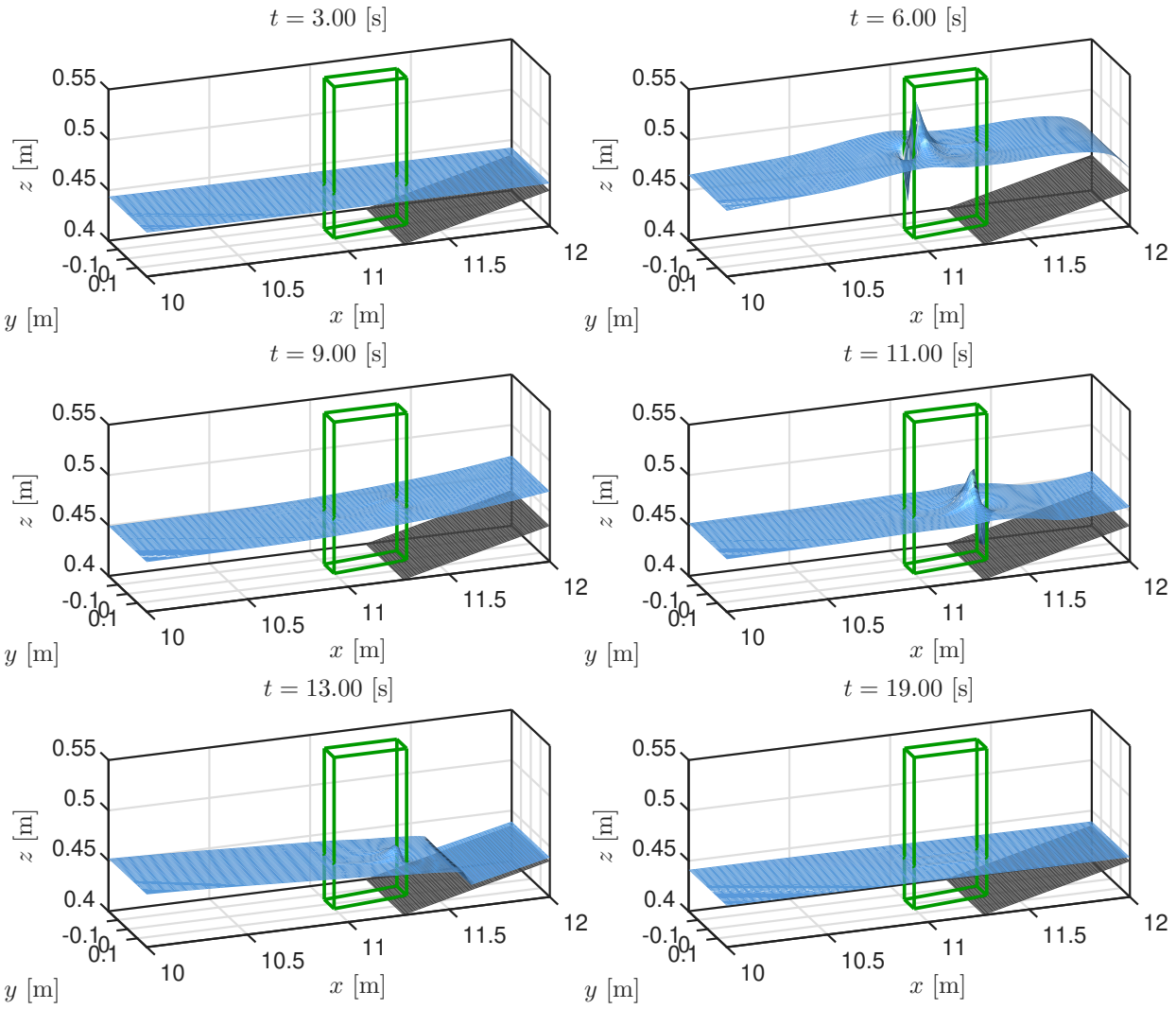

FIGURE 5. Example 3: snapshots of η in Case 3 of [27] at the downstream end of the vegetation ($x = 11.36$ m), with $H_0 = 0.44$ m and the forest confined to $y \in [-0.05, 0.05]$. Left: Wave reaching the front of the forest ($t = 6$ s). Right: Back flow of the forest ($t = 11$ s).

blockage diverts part of the flow laterally, producing marked transverse velocity components near the forest edges.

At $t = 11$ s, when the wave moves seaward, the interaction reverses: the forest again induces momentum accumulation at its downstream boundary and local high-velocity zones around it. This pattern of deceleration inside the vegetation and acceleration near its borders demonstrates how the forest simultaneously dissipates energy and redistributes the flow during both the advancing and receding phases of the wave.

The snapshots also reveal several complementary features of the flow–vegetation interaction. A pronounced velocity gradient forms between vegetated and non-vegetated areas, evidencing lateral

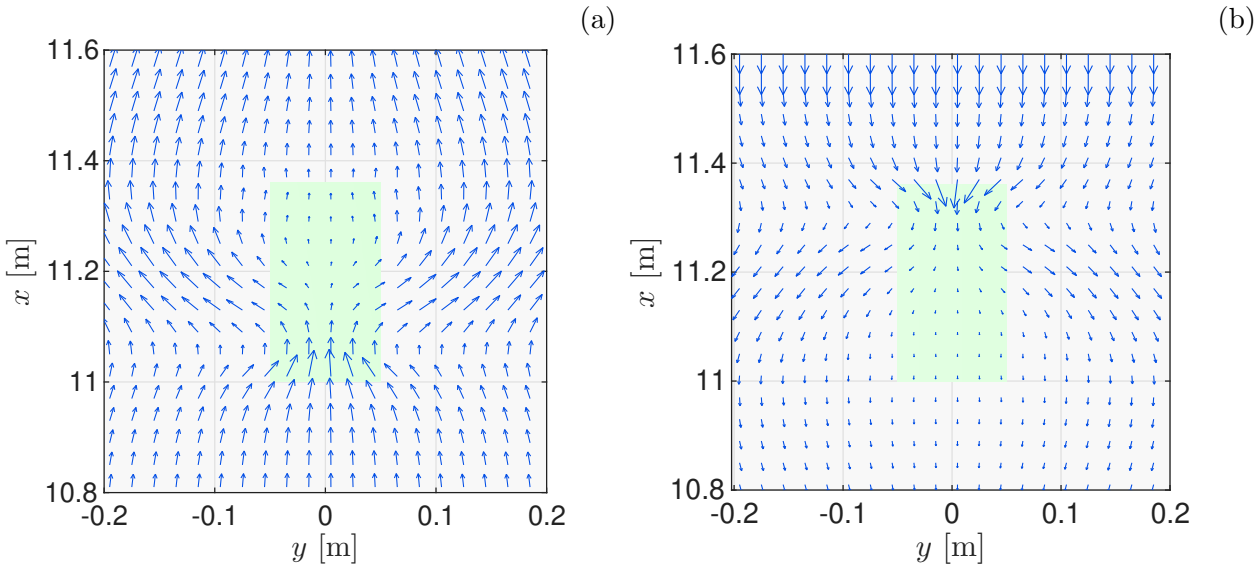

FIGURE 6. Example 3: snapshots of the mean horizontal velocity field $\boldsymbol{u} = (u, v)^{\mathrm{T}}$ in Case 3 of [27] at the downstream end of the vegetation ($x = 11.36$ m), with $H_0 = 0.44$ m and the forest confined to $y \in [-0.05, 0.05]$: (a) wave reaching the front of the forest ($t = 6$ s), (b) wave reaching the back of the forest ($t = 11$ s). Velocity vectors are normalized by $|\mathbf{u}|_{\max} \approx 10$ m/s.

flow redistribution. Partial reflection at the forest edge produces a localized rise in free-surface elevation immediately upstream, while the velocity within and behind the forest remains significantly lower than in unobstructed zones. Overall, these results highlight the dual hydrodynamic role of the forest as both a dissipative and deflective structure that shapes the spatial pattern of wave propagation.

As shown in Figure 7, at $t = 19$ s, the flow exhibits a distinct recirculation pattern near the beach. This phenomenon arises when water climbing the slop goes backward and interacts with the portion of the wave that is still propagating through the forest. The interaction generates backward flow and local vortices that are only resolved in a multilayer model; a single-layer approach fails to capture this complex vertical structure. The velocity vectors indicate a clear separation between backward-moving water near the slope and the advancing flow, forming a closed-loop circulation.

4.2.5. *Example 4: Influence of a uniform vegetation patch.* We consider a rectangular channel with spatial dimensions $x \in [-5, 25]$ m, $\quad y \in [-1, 1]$ m, and an initial solitary wave described by (4.1), with amplitude $\eta_0 = 0.0628$ m and still water level $h_0 = 0.44$ m. The channel bathymetry is defined as a piecewise function:

$$z_{\mathrm{b}}(x) = \begin{cases} 0, & x \le 10 \text{ m}, \\ 0.1(x - 10), & 10 < x \le 15 \text{ m}, \\ 0.5, & x > 15 \text{ m}. \end{cases} \tag{4.2}$$

The initial condition, along with the bathymetry and vegetation regions, is illustrated in Figure 8.

For the vegetation area, we consider two uniform configurations, both placed in the region $x \in [16, 17]$ m: the small vegetation area covers $y \in [-0.25, 0.25]$, while the larger configuration

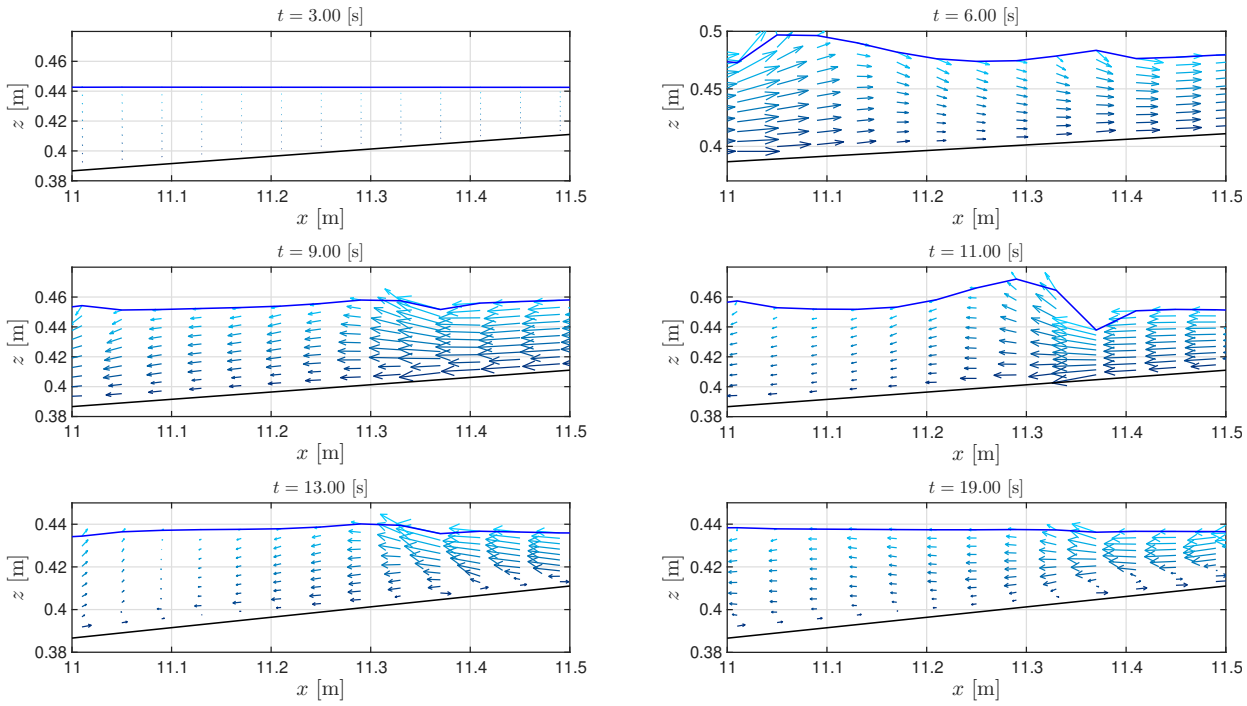

FIGURE 7. Example 3: velocity vector field $(u, w)^{\mathrm{T}}$ in the vertical (x, z)-plane at $y = 0$, at $t = 19\,\mathrm{s}$. The plot highlights the development of a recirculation zone near the beach. This phenomenon is only captured by a multilayer model, while a single-layer model cannot resolve it.

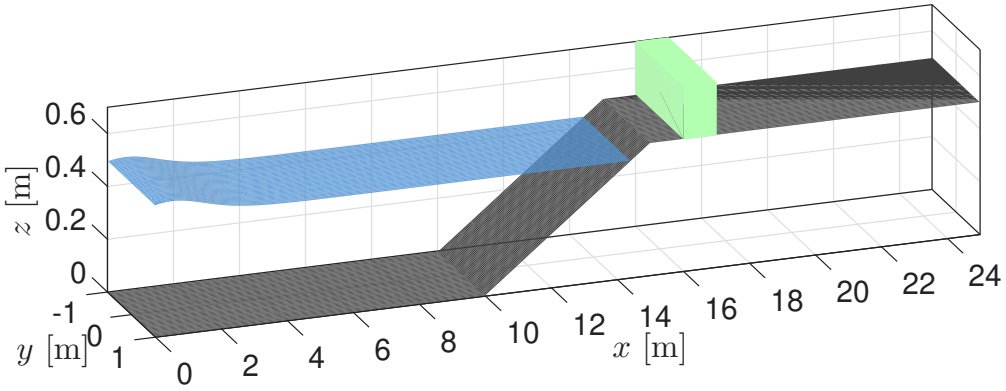

FIGURE 8. Example 4: initial condition of the channel, showing the bathymetry, the water level and the vegetation configuration for the full-width patch spans the entire y-range.

extends across the full width, $y \in [-1, 1]$. The stem diameter and density are identical for both configurations, with $d = 0.005$ m and $\rho = 1604$ stems/m^2, respectively.

Figure 9 presents the maximum water level at each point along the channel for simulations with and without vegetation. The presence of the forest significantly limits wave propagation into the vegetated region, whereas in the absence of vegetation the wave reaches further downstream. The

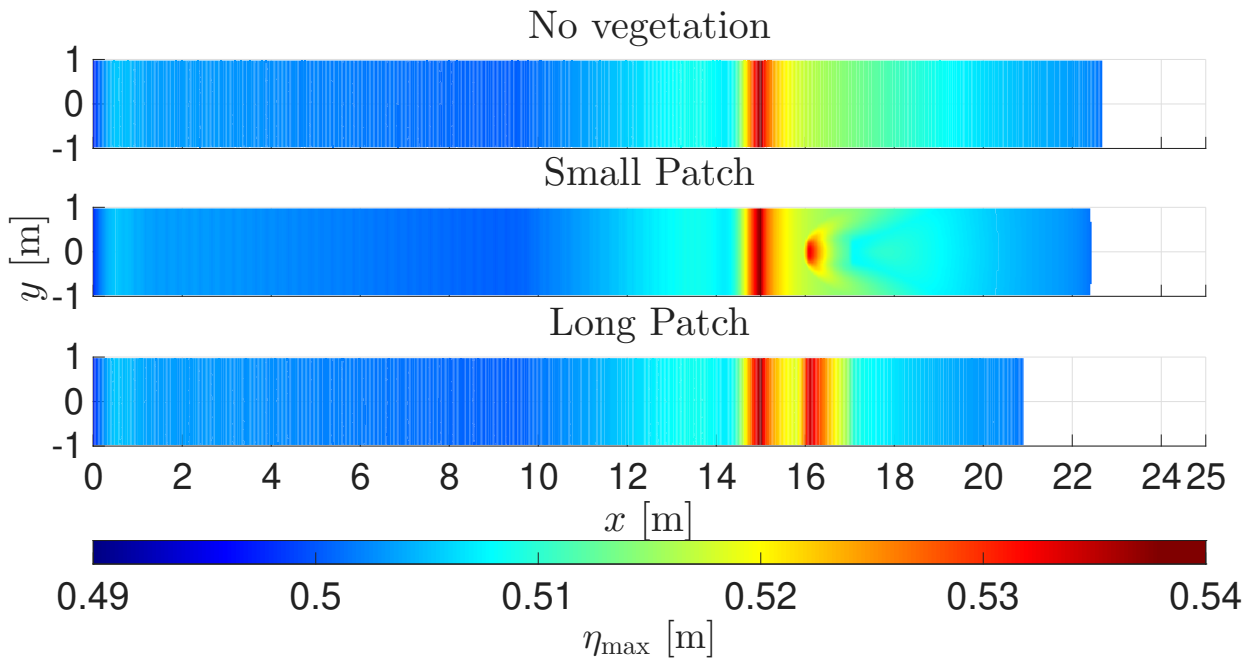

FIGURE 9. Example 4: maximum water level comparison. Top: simulation without vegetation. Middle: simulations whit a small vegetation patch. Bottom: simulation with a long vegetation patch. The forest reduces wave penetration and increases water level at the leading and trailing edges of the vegetated region.

water level increases locally at the forest front ($x = 16\,\mathrm{m}$), indicating flow accumulation caused by obstruction.

In the small patch configuration, we observe that the water flows around the vegetation, similar to what was seen in Example 3.2. This creates a protective region, or wake, behind the vegetation, which also reduces the extent to which the water propagates further downstream.

This behavior illustrates both energy dissipation and flow deflection due to the forest. The stems extract momentum from the incoming wave, reducing downstream propagation. These effects highlight the protective role of the vegetation in mitigating tsunami impact, in agreement with previous studies (e.g., Case 3 in [27]) where vegetation modifies wave amplitude and spatial structure.

4.3. **Example 5: Solitary wave on a conical island.** The objective of this study is to evaluate the extent to which surrounding forestation mitigates wave impact on a conical island. The physical benchmark considered here was originally conducted at the U.S. Army Engineer Research and Development Center, specifically within its Coastal and Hydraulic Laboratory [11]. The experimental configuration represents an idealized model of Babi Island, located in the Flores Sea.

In the laboratory setup, planar solitary waves with prescribed crest length and amplitude were generated using a directional wavemaker. The experimental basin measures $25 \times 30\mathrm{m}$, with a conical island positioned approximately at its center. The still water depth is $H = 0.32\,\mathrm{m}$. The island geometry is defined by a base diameter of 7.2 m, a top diameter of 2.2 m, and a height of 0.625 m, corresponding to a side slope of $1 : 4$. Free-surface elevations were recorded at four wave gauges (WG1–WG4) distributed circumferentially around the island (see Fig. 10).

For the numerical component, the computational domain spans $[-5, 23] \times [0, 28]\,\mathrm{m}$ with a uniform grid resolution of $\Delta x = \Delta y = 0.02\,\mathrm{m}$. Open (free-outflow) boundary conditions are prescribed along

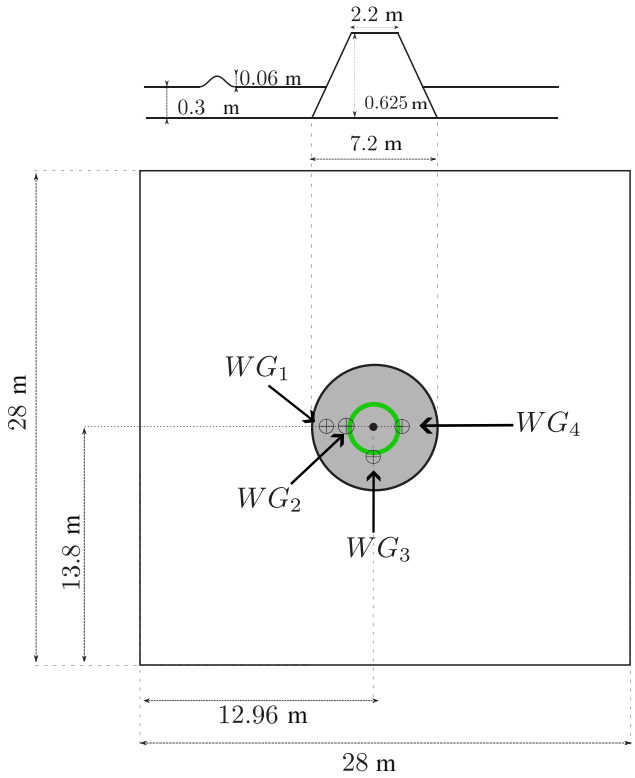

FIGURE 10. Example 5: Experimental configuration of the basin topography and wave gauge locations. The measurement points are positioned as follows: WG1 (9.36 m, 13.8 m), WG2 (10.36 m, 13.8 m), WG3 (12.96 m, 11.22 m), and WG4 (15.56 m, 13.8 m). Coordinates are given in meters relative to the basin reference frame. The green area represents the vegetation zone.

the domain boundaries. The initial condition for the free-surface elevation η and velocity field u corresponds to a solitary wave (Eq. (4.1)) with amplitude $A = 0.06\,\mathrm{m}$, initially centered at $x = 0$. The wave is propagated up to $t = 30\,\mathrm{s}$ using a Courant number CFL $= 0.9$ and gravitational acceleration $g = 9.81\,\mathrm{m/s^2}$. Bottom friction is modeled through a Manning roughness coefficient of $n = 0.015$.

To assess the ability of the numerical model to reproduce the physical experiment, the simulated results are compared against the experimental wave-gauge measurements. As we can see in Figure 11 the comparison between the simulation and the experimental data shows that the model captures both the amplitude and phase of the first waves .

For the present configuration, the test is extended by incorporating a toroidal vegetation belt surrounding the island. The vegetated region is modelled as an annular ring centred on the island, with external radius $r_2 = 3\,\mathrm{m}$ and internal radius $r_1 = 2\,\mathrm{m}$, measured from the island centre as we can see in Figure 12.

Within the annular vegetated region, four cases are considered. In Case 1, we assume a uniform vegetation density of $n = 800\,\mathrm{trees/m^2}$, where each tree is modeled as a rigid cylindrical element with radius $d = 0.005\,\mathrm{m}$. In Case 2 we consider a reduced vegetation density of $n = 400\,\mathrm{trees/m^2}$, combined with an increased cylinder radius of $d = 0.01\,\mathrm{m}$. Case 3 is based on the same density and cylinder radius as Case 2 ($n = 400\,\mathrm{trees/m^2}$, $d = 0.01\,\mathrm{m}$), but with a maximum tree height of

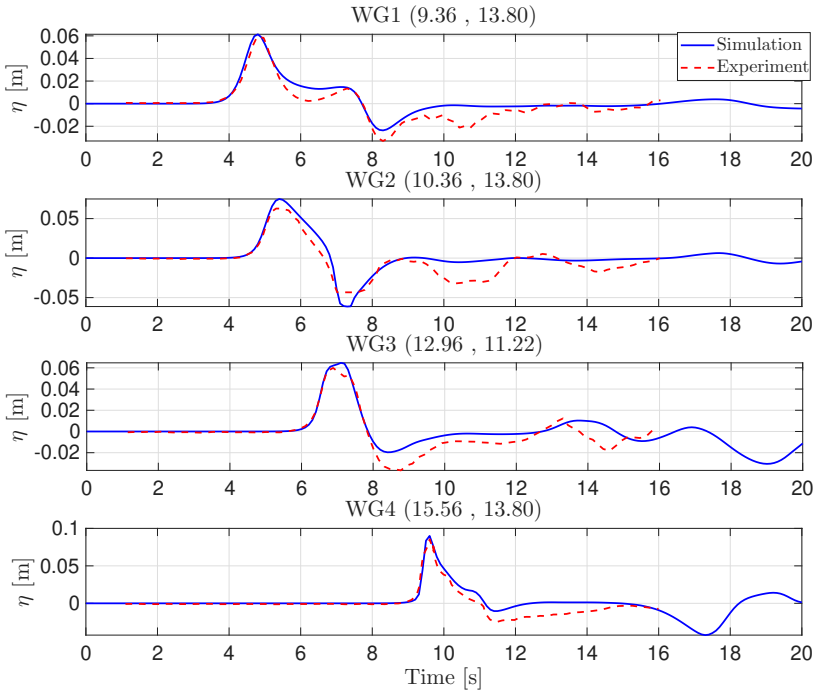

FIGURE 11. Example 5: simulated and experimental free-surface elevation time series at the wave gauges.

0.03 m. Finally, in Case 4 we take the same density and cylinder radius as in Case 2 but a maximum tree height of 0.09 m.

For all configurations, $N = 10$ vertical layers are employed. As shown in Figure 13, the differences between Case 1 and Case 2 are minimal, whereas both cases exhibit significant reductions compared to the non-vegetated configuration. In contrast, comparing Case 3 and Case 4 (Figure 14) reveals noticeable differences in both the minimum and maximum water levels, reflecting the effect of varying maximum tree height. Additionally, we examined Case 3 using only a single vertical layer, with constant tree diameter. As expected, the single-layer model tends to overestimate the ability of the vegetation to mitigate waves, since it cannot accurately capture the vertical structure of the trees, particularly the maximum height.

We define the attenuation factor as

$$\beta = 1 - \frac{H_{\text{veg}}}{H_{\text{ref}}}, \tag{4.3}$$

where H_{veg} and H_{ref} are the maximum wave heights measured at each gauge in the vegetated and non-vegetated simulations, respectively. Figure 15 shows the computed attenuation factors at the four wave gauges for Case 1. The results indicate that the wave height reduction ranges between approximately 10% and 40%, with the greatest attenuation observed at Gauge 4 and the smallest at Gauge 1.

As illustrated in Figure 16, the vegetation acts as a natural barrier. At $t = 0$ s, both the reference and vegetated cases exhibit identical initial conditions. By $t = 5$ s, the presence of vegetation begins to induce noticeable differences compared with the reference simulation, as the long-wave soliton interacts with the forest and generates partial reflection. At $t = 8$ s, the vegetation causes a local increase in the water level upstream of the island due to the blockage of the wave passage. Finally,

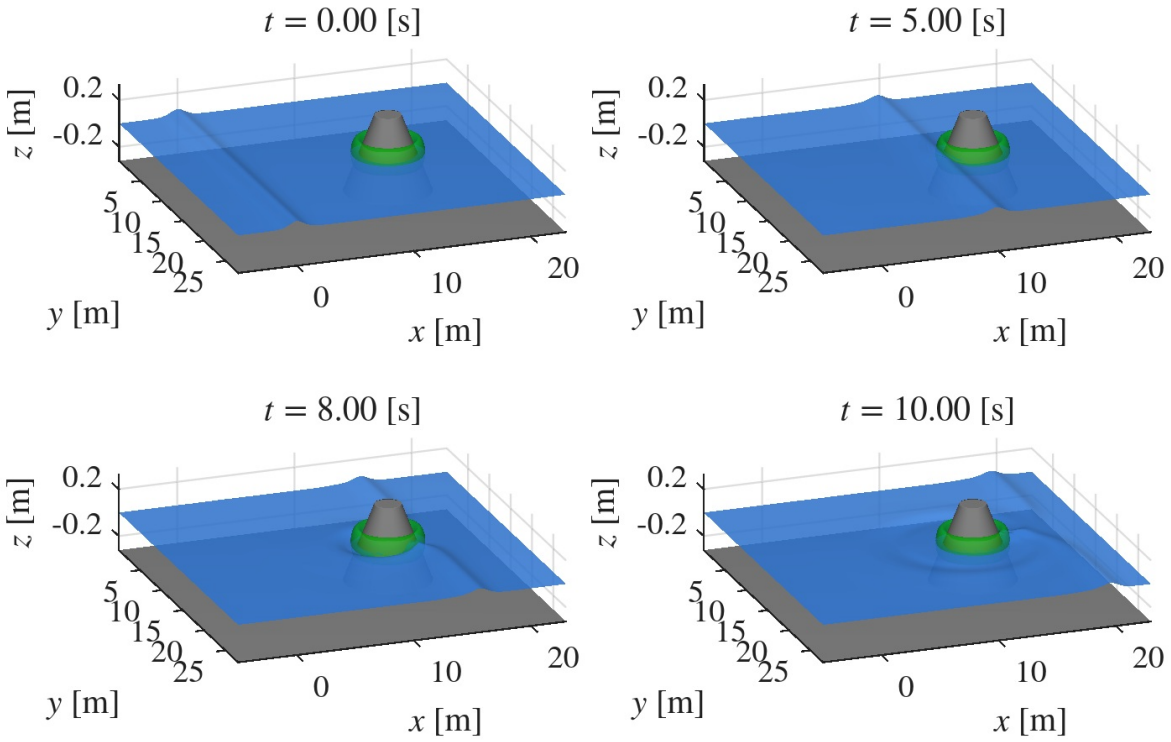

FIGURE 12. Example 5: Snapshots of the difference in free-surface elevation case without vegetation at four different times.

at $t = 10\,\mathrm{s}$, the region downstream of the island exhibits a lower water level relative to the reference case, showing the protective effect of the vegetative barrier.

5. Conclusions and future work

This work presents a two-dimensional multilayer non-hydrostatic shallow-water model designed to simulate tsunami propagation and tsunami–vegetation interactions with improved physical realism. The model combines a multilayer depth-averaged formulation with a projection method for the non-hydrostatic pressure, providing a robust and computationally efficient framework for representing vertically structured hydrodynamics in coastal environments.

The proposed approach captures several flow features that cannot be reproduced with classical hydrostatic or single-layer models, including vertical recirculation, return flows near the shoreline, and lateral redistribution of momentum as the tsunami interacts with vegetated regions. The multilayer structure enables the inclusion of vertical variability in drag, inertia, and porosity, allowing the model to represent the influence of vegetation along the water column more accurately. This results in improved predictions of wave attenuation, energy dissipation, and flow deformation within and around vegetated belts. The elliptic projection for the non-hydrostatic pressure further stabilizes the vertical velocity structure and enhances the representation of steep gradients and transient flow features.

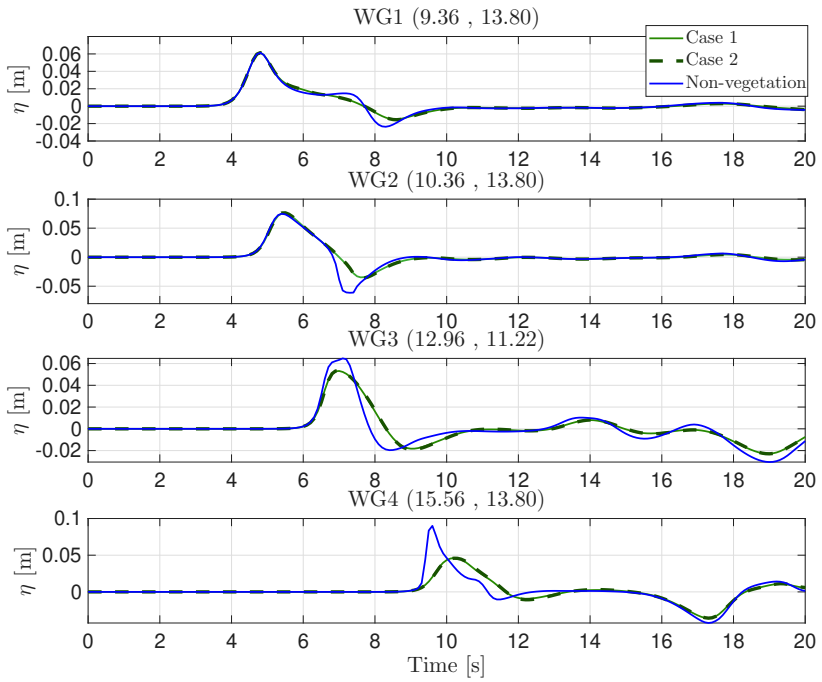

FIGURE 13. Example 5: simulated free-surface elevation time series at the wave gauges for the three configurations: non-vegetated case, Case 1 ($n = 800$ trees/m^2, $d = 0.005$ m), and Case 2 ($n = 400$ trees/m^2, $d = 0.01$ m).

The numerical experiments demonstrate that, while single-layer depth-averaged models remain suitable for capturing bulk tsunami propagation, a multilayer non-hydrostatic formulation is essential for resolving internal flow structure and layer-to-layer energy exchanges, both of which determine the damping efficiency of coastal forests. The model therefore provides a valuable tool for assessing the protective function of vegetation belts and for supporting coastal management strategies that rely on nature-based protection measures.

The outcomes of this study highlight the importance of incorporating vertical resolution and non-hydrostatic effects into depth-averaged models when representing the interaction between tsunamis and coastal vegetation. Beyond its methodological advances, the model offers practical capabilities for evaluating the role of native vegetation in mitigating tsunami hazards and promoting sustainable, ecosystem-based coastal defense strategies.

Several directions for future research emerge from this work. One promising avenue is the development of a unified two-dimensional hydro-morphodynamic framework that couples the present multilayer non-hydrostatic model with sediment transport processes to study tsunami-induced erosion in vegetated coastal zones. Numerical enhancements such as adaptive mesh refinement, implicit–explicit time integration, and high-order reconstructions would further improve accuracy and computational efficiency. Finally, extending the model to simulate tsunami run-up and other nearshore processes would broaden its applicability and support more comprehensive risk assessments in coastal engineering and management.

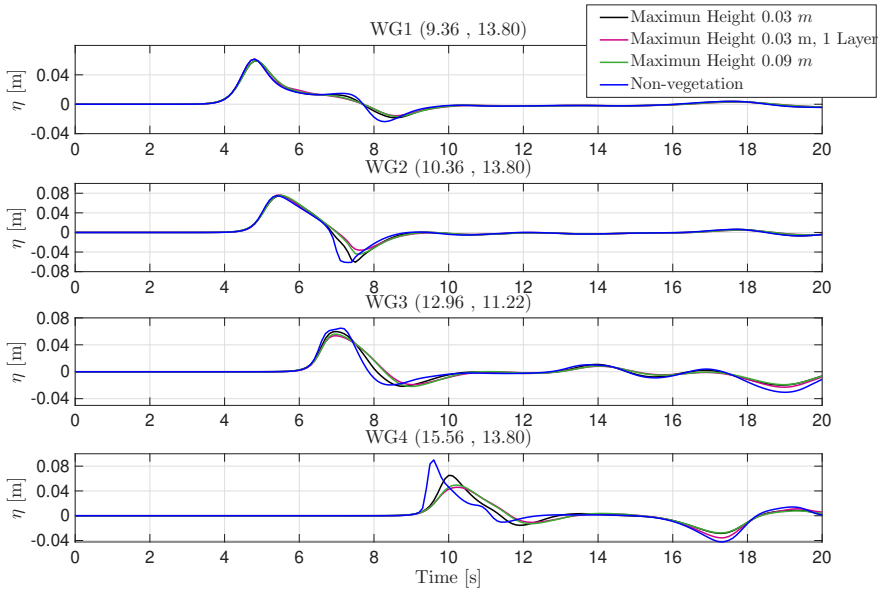

FIGURE 14. Example 5: simulated free-surface elevation time series at the wave gauges for Cases 3 and 4, both with a vegetation density of $n = 400\,\text{trees/m}^2$ and cylinder radius $d = 0.01\,\text{m}$, showing the effect of maximum tree height: Case 3 with 0.03 m and Case 4 with 0.09 m.

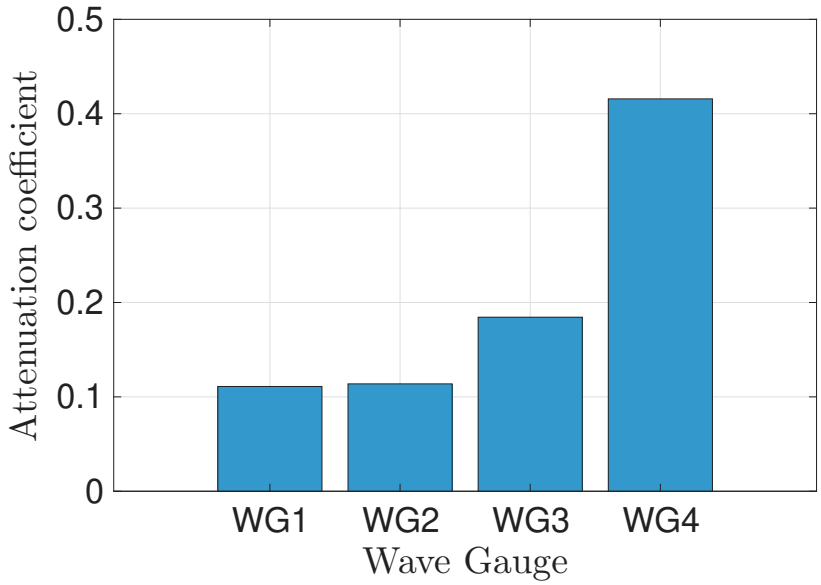

FIGURE 15. Example 5: wave attenuation coefficient at the four gauges induced by the vegetated belt, computed relative to the non-vegetated configuration.

ACKNOWLEDGEMENTS

We acknowledge support by ANID (Chile) via projects Fondecyt 1250676 and Centro de Modelamiento Matemático (BASAL project FB210005) (both to RB) and Becas Doctorado Nacional

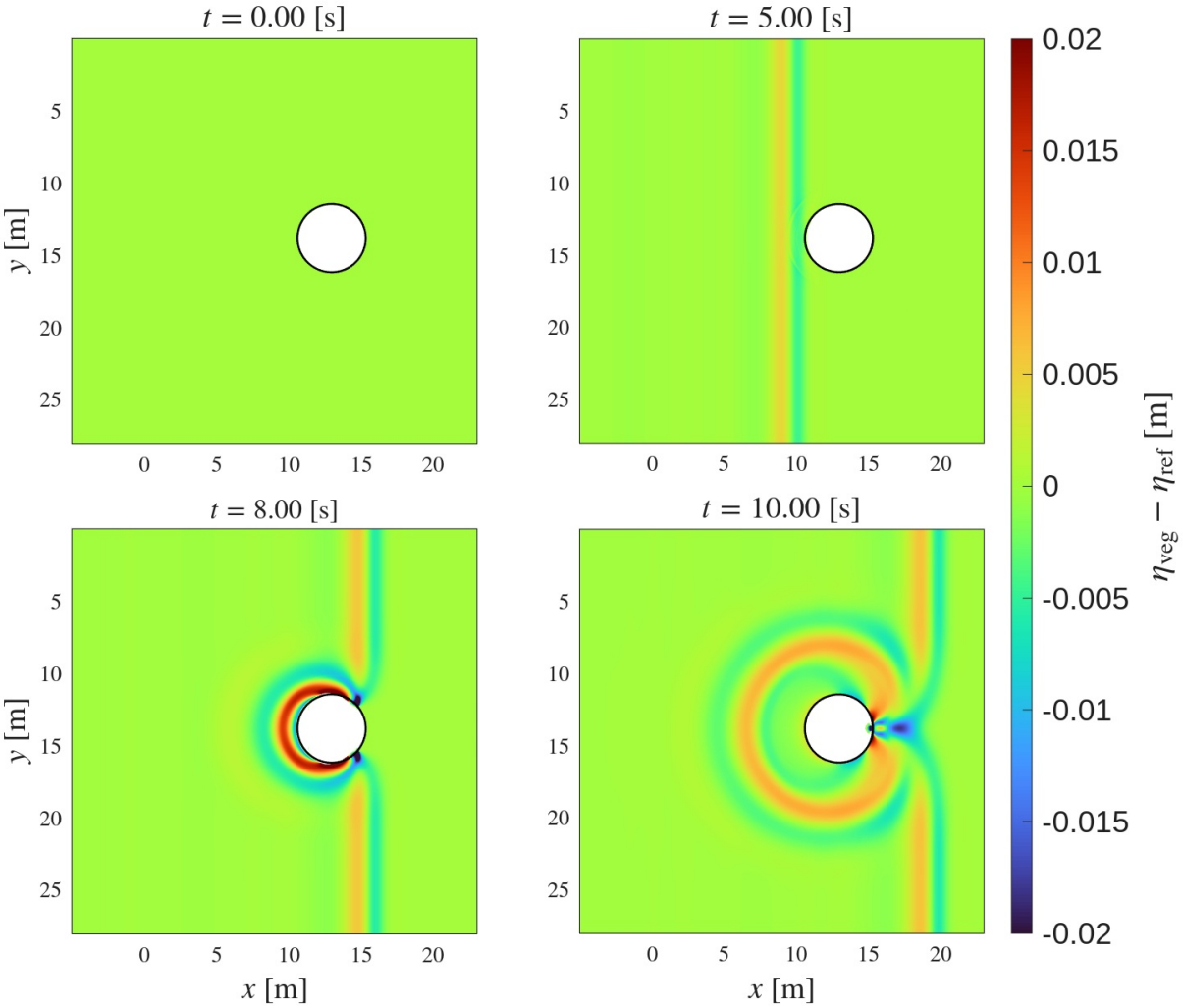

FIGURE 16. Example 5: snapshots of the difference in free-surface elevation between the vegetation case η_{veg} and the baseline case without vegetation η_{ref} at four different times.

2021, folio 21211457 (to JM), Junta de Andalucía research project ProyExcel_00525, by the European Union - NextGenerationEU program, and by grants PID2022-137637NB-C21 and PID2022-137637NB-C22 funded by MCIN/AEI/10.13039/
501100011033 and "ERDF A way of making Europe.

Appendix A. Forest forces in the multi-layer system

Vegetation effects are introduced in a layer-wise form via layer-specific geometric and vegetation averages. As in the one-dimensional formulation [12], let $d(\zeta)$ denote the tree diameter at height ζ measured from the bed z_b, and let $c_\mathrm{tr}(\zeta)$ and $c_\mathrm{le}(\zeta)$ be the trunk- and leaf-shape factor, respectively. For each layer α we define the layer-averaged diameter $\bar{d}_\alpha$ and the vegetation coefficient $(\overline{c_\mathrm{tr}c_\mathrm{le}})_\alpha$ by

$$\bar{d}_\alpha \coloneqq \frac{1}{h_\alpha}\int_{z_{\alpha-1/2}-z_\mathrm{b}}^{z_{\alpha+1/2}-z_\mathrm{b}} d(\zeta)\,\mathrm{d}\zeta, \qquad (\overline{c_\mathrm{tr}c_\mathrm{le}})_\alpha \coloneqq \frac{1}{h_\alpha}\int_{z_{\alpha-1/2}-z_\mathrm{b}}^{z_{\alpha+1/2}-z_\mathrm{b}} c_\mathrm{tr}(\zeta)c_\mathrm{le}(\zeta)\,\mathrm{d}\zeta. \tag{1.1}$$

The definition of $\bar{d}_\alpha$ allows us to define thre effective frontal area $A_{\mathrm{v},\alpha} \coloneqq h_\alpha \bar{d}_\alpha$ and the transverse area $A_{\mathrm{t},\alpha} \coloneqq \pi \bar{d}_\alpha^2/4$ of a single tree in layer α.

Following the experimental parametrization used in the one-dimensional study, we introduce a base (Reynolds number-dependent) drag coefficient $C_\mathrm{D}(\mathrm{Re})$ according to [35]:

$$C_\mathrm{D}(\mathrm{Re}) \coloneqq \begin{cases} 1.2 & \text{if } \mathrm{Re} \le 2\times 10^5, \\ 1.2 - 0.5\left(\dfrac{\mathrm{Re}}{3\times 10^5} - \dfrac{2}{3}\right) & \text{if } 2\times 10^5 < \mathrm{Re} \le 5\times 10^5, \\ 0.7 & \text{if } \mathrm{Re} > 5\times 10^5, \end{cases} \tag{1.2}$$

where the Reynolds number Re is replaced by a layer-wise Reynolds number Re_α that is computed based on the layer velocity magnitude, namely $\mathrm{Re}_\alpha \coloneqq \|\boldsymbol{u}_\alpha\|\bar{d}_\alpha/\nu_\mathrm{water}$, where $\nu_\mathrm{water} = 1.19 \times 10^{-6}\,\mathrm{m}^2/\mathrm{s}$ is the kinematic viscosity of water. The layer-specific drag coefficient used in the drag force is the base coefficient modulated by the trunk/leaf factor, i.e.

$$C_{\mathrm{D},\alpha} = C_\mathrm{D}(\mathrm{Re}_\alpha)(\overline{c_\mathrm{tr}c_\mathrm{le}})_\alpha. \tag{1.3}$$

References

[1] J. Akiyama and Y. Fukushima. Entrainment of noncohesive bed sediment into suspension. Technical Report External Memo. No. 175, Minneapolis, USA, 1985.

[2] E. Audusse. A multilayer saint-venant model: derivation and numerical validation. *Discrete Contin. Dyn. Syst. Ser. B*, 5:189–214, 2005.

[3] E. Audusse, F. Bouchut, M. Bristeau, R. Klein, and B. Perthame. A fast and stable well-balanced scheme with hydrostatic reconstruction for shallow water flows. *SIAM Journal on Scientific Computing*, 25(6):2050–2065, jan 2004.

[4] E. Audusse, F. Bouchut, M.-O. Bristeau, R. Klein, and B. Perthame. A fast and stable well-balanced scheme with hydrostatic reconstruction for shallow water flows. *SIAM J. Sci. Comput.*, 25:2050–2065, 2004.

[5] E. Audusse, M. Bristeau, B. Perthame, and J. Sainte-Marie. A multilayer Saint-Venant system with mass exchanges for shallow water flows. derivation and numerical validation. *ESAIM: Mathematical Modelling and Numerical Analysis*, 45(1):169–200, jun 2010.

[6] E. Audusse, M. Bristeau, B. Perthame, and J. Sainte-Marie. A multilayer saint-venant system with mass exchanges for shallow water flows. derivation and numerical validation. *ESAIM: Math. Model. Numer. Anal.*, 45:169–200, 2011.

[7] E. Audusse and M.-O. Bristeau. Finite-volume solvers for a multilayer saint-venant system. *Int. J. Appl. Math. Comput. Sci.*, 17:311–319, 2007.

[8] E. Audusse, M.-O. Bristeau, and A. Decoene. Numerical simulations of 3d free surface flows by a multilayer saint-venant model. *Int. J. Numer. Methods Fluids*, 56:331–350, 2008.

[9] E. Audusse, M.-O. Bristeau, M. Pelanti, and J. Sainte-Marie. Approximation of the hydrostatic Navier-Stokes system for density stratified flows by a multilayer model: kinetic interpretation and numerical solution. *J. Comput. Phys.*, 230(9):3453–3478, 2011.

[10] E. Audusse, M.-O. Bristeau, M. Pelanti, and J. Sainte-Marie. Approximation of the hydrostatic navier–stokes system for density stratified flows by a multilayer model: kinetic interpretation and numerical solution. *J. Comput. Phys.*, 230:3453–3478, 2011.

[11] M. J. Briggs, C. E. Synolakis, G. S. Harkins, and D. R. Green. Laboratory experiments of tsunami runup on a circular island. *Pure and Applied Geophysics PAGEOPH*, 144(3-4):569 – 593, 1995. Cited by: 253.

[12] R. Bürger, E. D. Fernández-Nieto, and J. Moya. A multilayer shallow water model for tsunamis and coastal forest interaction. *ESAIM: Math. Model. Numer. Anal.*, 59(2):1113–1144, 2025.

[13] R. Bürger, E. D. Fernández-Nieto, and V. Osores. A dynamic multilayer shallow water model for polydisperse sedimentation. *ESAIM: Math. Model. Numer. Anal.*, 53:1391–1432, 2019.

[14] R. Bürger, E. D. Fernández-Nieto, and V. Osores. A multilayer shallow water approach for polydisperse sedimentation with sediment compressibility and mixture viscosity. *J. Sci. Comput.*, 85:article 49 (40pp), 2020.

[15] M. J. Castro and E. Fernández-Nieto. A class of computationally fast first order finite volume solvers: Pvm methods. *SIAM J. Sci. Comput.*, 34:A2173–A2196, 2012.

[16] M. J. Castro, A. M. F. Ferreiro, J. A. García-Rodríguez, J. M. González-Vida, J. Macías, C. Parés, and M. E. Vázquez-Cendón. The numerical treatment of wet/dry fronts in shallow flows: application to one-layer and two-layer systems. *Math. Comput. Modelling*, 42:419–439, 2005.

[17] M. J. Castro, T. Morales de Luna, and C. Parés. Well-Balanced Schemes and Path-Conservative Numerical Methods. In R. Abgrall and C.-W. Shu, editors, *Handbook of Numerical Analysis*, volume 18 of *Handbook of Numerical Methods for Hyperbolic Problems Applied and Modern Issues*, pages 131–175. Elsevier, 2017. DOI: 10.1016/bs.hna.2016.10.002.

[18] A. J. Chorin. The numerical solution of the navier-stokes equations for an incompressible fluid. *Bull. Am. Math. Soc.*, 73:928–931, 1967.

[19] A. J. Chorin. Numerical solution of the navier-stokes equations. *Math. Comput.*, 22:745–762, 1968.

[20] M. J. C. Díaz, J. Gallardo, and C. Parés. High order finite volume schemes based on reconstruction of states for solving hyperbolic systems with nonconservative products. applications to shallow-water systems. *Math. Comput.*, 75:1103–1134, 2006.

[21] C. Escalante, T. Morales de Luna, and M. Castro. Non-hydrostatic pressure shallow flows: Gpu implementation using finite volume and finite difference scheme. *Appl. Math. Comput.*, 338:631–659, 2018.

[22] E. Fernández-Nieto, J. Garres-Díaz, A. Mangeney, and G. Narbona-Reina. A multilayer shallow model for dry granular flows with the $\mu(i)$-rheology: Application to granular collapse on erodible beds. *J. Fluid Mech.*, 798:643–681, 2016.

[23] E. D. Fernández-Nieto, E. H. Koné, T. M. de Luna, and R. Bürger. A multilayer shallow water system for polydisperse sedimentation. *J. Comput. Phys.*, 238:281–314, 2013.

[24] E. D. Fernández-Nieto, E. H. Koné, and T. C. Rebollo. A multilayer method for the hydrostatic navier–stokes equations: a particular weak solution. *J. Sci. Comput.*, 60:408–437, 2014.

[25] E. D. Fernández-Nieto, M. Parisot, Y. Penel, and J. Sainte-Marie. A hierarchy of dispersive layer-averaged approximations of Euler equations for free surface flows. *Commun. Math. Sci.*, 16(5):1169–1202, 2018.

[26] A. Harten, P. D. Lax, and B. van Leer. On upstream differencing and Godunov-type schemes for hyperbolic conservation laws. *SIAM Rev.*, 25(1):35–61, 1983.
[27] K. Iimura and N. Tanaka. Numerical simulation estimating effects of tree density distribution in coastal forest on tsunami mitigation. *Ocean Engrg.*, 54:223–232, 2012.
[28] A. Kurganov and G. Petrova. A second-order well-balanced positivity preserving central-upwind scheme for the saint-venant system. *Commun. Math. Sci.*, 5:133–160, 2007.
[29] R. J. LeVeque. *Finite volume methods for hyperbolic problems*. Cambridge Texts in Applied Mathematics. Cambridge University Press, Cambridge, 2002.
[30] Lord Rayleigh (J. W. Strutt). On waves. *Philosophical Magazine*, 1:257–279, 1876.
[31] G. D. Maso, P. G. LeFloch, and F. Murat. Definition and weak stability of nonconservative products. *J. Math. Pures Appl.*, 74:483–548, 1995.
[32] C. Parés. Numerical methods for nonconservative hyperbolic systems: a theoretical framework. *SIAM J. Numer. Anal.*, 44(1):300–321, jan 2006.
[33] C. Parés and M. Castro. On the well-balance property of Roe's method for nonconservative hyperbolic systems. Applications to shallow-water systems. *ESAIM: Mathematical Modelling and Numerical Analysis*, 38(5):821–852, sep 2004.
[34] M. Parisot. Entropy-satisfying scheme for a hierarchy of dispersive reduced models of free surface flow. *Int. J. Numer. Methods Fluids*, 91(10):509–531, 2019.
[35] R. Rodríguez, P. Encina, M. Espinosa, and N. Tanaka. Field study on planted forest structures and their role in protecting communities against tsunamis: experiences along the coast of the Biobío region, Chile. *Landscape Ecol. Eng.*, 12:1–12, 2016.
[36] J. Sainte-Marie. Vertically averaged models for the free surface non-hydrostatic euler system: derivation and kinetic interpretation. *Math. Models Methods Appl. Sci.*, 21:459–490, 2011.
[37] C. E. Sánchez, E. D. Fernández-Nieto, T. M. de Luna, Y. Penel, and J. Sainte-Marie. Numerical simulations of a dispersive model approximating free-surface euler equations. *J. Sci. Comput.*, 89:article 55 (32pp), 2021.
[38] N. Shuto. The effectiveness and limit of tsunami control forests. *Coastal Engrg. Japan*, 30:143–153, 1987.
[39] N. Tanaka. Effectiveness and limitations of vegetation bioshield in coast for tsunami disaster mitigation. In N.-A. Mörner, editor, *The Tsunami Threat — Research and Technology*, chapter 9, pages 161–178. InTech, Rijeka, Croatia, 2011.
[40] N. Tanaka, Y. Sasaki, M. I. M. Mowjood, K. B. S. N. Jinadasa, and S. Homchuen. Coastal vegetation structures and their functions in tsunami protection: Experience of the recent Indian Ocean tsunami. *Landscape Ecol. Eng.*, 3:33–45, 2007.
[41] R. Témam. Sur l'approximation de la solution des équations de Navier-Stokes par la méthode des pas fractionnaires (I). *Arch. Rational Mech. Anal.*, 32(2):135–153, Jan. 1969.
[42] E. F. Toro. *Computational Algorithms for Shallow Water Equations*. Springer Nature, Cham, Switzerland, 2nd edition, 2024.
[43] H. Yanagisawa, S. Koshimura, K. Goto, T. Miyagi, F. Imamura, A. Ruangrassamee, and C. Tanavud. The reduction effects of mangrove forest on a tsunami based on field surveys at pakarang cape, thailand and numerical analysis. *Estuar. Coast. Shelf Sci.*, 81:27–37, 2009.

Centro de Investigación en Ingeniería Matemática (CI^{2}MA)

PRE-PUBLICACIONES 2026

2026-03 Sergio Caucao, Gabriel N. Gatica, Adrian Suarez, Ivan Yotov: *A skew-symmetry-based mixed formulation for an Oseen-type Kelvin–Voigt–Brinkman–Forchheimer model*

2026-04 Akbar Davoodi, Diana Piguet, Hanka Rada, Nicolás Sanhueza-Matamala: *The asymptotic version of the Erdős–Sós conjecture and beyond*

2026-05 Rodrigo Abarca Del Rio, Fernando Campos, Cristóbal Caro-Ramírez, Jean François Cretaux, Daniel Moreira, Alfredo Ribeiro Neto, Jonas Felipe Santos De Souza, Mauricio Sepúlveda: *First insights into the performance of the SWOT Level 2 River Single-Pass Vector Data Product in rivers with complex morphology: application to the Bíobío River basin, Chile*

2026-06 Juan José Maulén, Fernando Roldán, Cristian Vega: *Relaxed and inertial nonlinear Forward-Backward algorithm*

2026-07 Luis Briceño-Arias, Fernando Roldán: *Optimal leveraging of smoothness and strong convexity for Peaceman-Rachford splitting*

2026-08 Fahim Aslam, Jianghao Hao, Iqra Kanwal, Mauricio Sepúlveda: *Stability and finite-time blow-up for a fractionally damped nonlinear plate equation: numerical and analytical insights*

2026-09 Fahim Aslam, Zayd Hajjej, Jianghao Hao, Iqra Kanwal, Mauricio Sepúlveda, Rodrigo Véjar: *Stability and blow-up for a suspension bridge plate model with fractional damping and memory*

2026-10 Aníbal Coronel, Fernando Huancas, Mauricio Sepúlveda: *Identification of a power-like reaction term in a reaction-diffusion SIS model*

2026-11 Esteban Henriquez, Manuel Solano: *An unfitted HDG method for a distributed optimal convection-diffusion control problem*

2026-12 Sergio Caucao, Gabriel N. Gatica, Luis F. Gatica, Cristian Inzunza: *A priori and a posteriori error analysis of a mixed FEM for stationary convective Brinkman-Forchheimer flows with variable porosity*

2026-13 Jessika Camaño, Ricardo Oyarzúa, Katherine Rojo, Segundo Villa-Fuentes: *A mixed finite element method based on pseudostress and stream-function for the Navier–Stokes problem in 2D*

2026-14 Raimund Bürger, Cipriano Escalante, Enrique D. Fernández Nieto, Jorge Moya: *A two-dimensional multilayer shallow water model of tsunami-forest interaction*

Para obtener copias de las Pre-Publicaciones, escribir o llamar a: Director, Centro de Investigación en Ingeniería Matemática, Universidad de Concepción, Casilla 160-C, Concepción, Chile, Tel.: 41-2661324, o bien, visitar la página web del centro: `http://www.ci2ma.udec.cl`




Centro de Investigación en
Ingeniería Matemática (CI²MA)
Universidad de Concepción

Casilla 160-C, Concepción, Chile
Tel.: 56-41-2661324/2661554/2661316
http://www.ci2ma.udec.cl